# Resonance fluorescence from a single quantum Dot in a nanopost optical cavity

Maxime Gaignard, Matteo Finazzer, Clemens Spinnler, Giang Nguyen, Saptarshi Kotal, Alberto Artioli, Yann Genuist, Niels Gregersen, Jean-Philippe Poizat, Jean-Michel Gérard, et al.

# Resonance fluorescence from a single quantum dot in a nanopost optical cavity

Maxime Gaignard,[†,‖] Matteo Finazzer,[†,‖] Clemens Spinnler,[‡] Giang N. Nguyen,[‡] Saptarshi Kotal,[†] Alberto Artioli,[†] Yann Genuist,[¶] Niels Gregersen,[§] Jean-Philippe Poizat,[¶] Jean-Michel Gérard,[†] Richard J. Warburton,[‡] and Julien Claudon[*,†]

†*Univ. Grenoble Alpes, CEA, Grenoble INP, IRIG, PHELIQS, "Nanophysique et semiconducteurs" group, F-38000 Grenoble, France*

‡*Department of Physics, University of Basel, Klingelbergstrasse 82, CH-4056 Basel, Switzerland*

¶*Univ. Grenoble Alpes, CNRS, Grenoble INP, Institut Néel, "Nanophysique et semiconducteurs" group, F-38000 Grenoble, France*

§*DTU Electro, Department of Electrical and Photonics Engineering, 2800 Kongens Lyngby, Denmark*

‖*M.G. and M.F. contributed equally to this work*

E-mail: julien.claudon@cea.fr

**Abstract**

Scaling-up photonic quantum technologies will require the parallel operation of on-demand sources of identical single photons. In this context, broadband photonic structures embedding a single quantum dot (QD) are particularly appealing, as optimal source performance can be maintained upon QD spectral tuning. The nanopost —

a nanocavity built with a segment of photonic wire — offers a broadband Purcell effect and a directive output beam. So far however, QD-nanopost devices were only characterized using non-resonant optical excitation. Here, we employ a continuous wave laser to resonantly drive a single QD in a nanopost and detect its resonance fluorescence. Even though the nanopost introduces a significant optical roughness at the scale of the focused laser spot, a cross-polarization scheme leads to an excellent rejection of the excitation laser. We extensively characterize the QD optical emission by combining linescans and intensity correlation measurements, which are jointly analyzed with an analytical model. The emission features a pronounced antibunching ($g^{(2)}(0) = 0.02$), close to the one of an ideal two-level system. For small driving powers, the homogeneous (total) spectral linewidth is a factor of 1.4 (5) above the Fourier limit. Combined with future device improvements, these results mark an important step towards the realization of bright and widely-tunable sources of indistinguishable single photons.

## Keywords

Quantum dot; Nanopost; Broadband optical nanocavity; Purcell effect; Resonance fluorescence; Single-photon source; Intensity autocorrelation; Spectral diffusion

## Introduction

Resonance fluorescence results from the scattering of a continuous wave laser by an optically-active two-level system, such as a semiconductor quantum dot (QD). Despite its simplicity, this fundamental quantum optics process entails a wealth of intriguing phenomena.[1–7] Resonance fluorescence also plays a key role in the development of QD-based photonic quantum technologies.[8] By minimizing the excitation of uncontrolled degrees of freedom associated with the host matrix, it leads to the emission of highly-coherent photons,[9–11] a feature main-

tained in the pulsed excitation regime.[12,13] In addition, it enables a fine characterization of residual noise sources acting on the emitter,[14–20] paving the way towards further improvements of the photon coherence. In practice, separating the QD emission from the excitation laser represents a significant experimental challenge. Efficient laser rejection can be achieved using various techniques,[21] including path separation[9,22–24] or polarization-based dark field.[25–28] In the latter, one detects the signal component that is cross-polarized with respect to the driving laser. This strategy leads to an excellent laser rejection for planar structures,[28–30] and for photonic structures featuring a flat, micron-scale top facet, such as micropillars[12,13] and photonic trumpets.[18,31] To date, demonstrations with structures smaller than the free-space wavelength are still extremely scarce. One work reports resonance fluorescence from a single QD embedded in a needle-like photonic wire antenna,[27] albeit with relatively modest signal-to-background levels. Very recently, clean laser rejection was demonstrated in a similar system under pulsed resonant excitation,[32] however without addressing the spectral properties of the emitted photons.

In this Article, we use a continuous wave laser to resonantly drive a self-assembled QD that is embedded in a nanopost optical cavity, and detect the QD resonance fluorescence. The nanopost is designed for free-space emission and offers a broadband acceleration of spontaneous emission,[33,34] which is appealing for the realization of tunable sources of indistinguishable single photons and bright sources of entangled-photon pairs. This cylindrical photonic structure is made of a high-index material and features a diameter of 250 nm, typically four times smaller than the focused laser spot. Yet, a cross-polarization scheme leads to an excellent rejection of the driving laser. We leverage resonance fluorescence to perform a comprehensive characterization of the QD emission dynamics, over a broad range of timescales. Specifically, we perform linescans and intensity autocorrelation measurements and introduce a fully analytical model to interpret the data. The QD emission features a nearly-perfect antibunching and a close-to-lifetime-limited dephasing time. Measurements also reveal a moderate spectral diffusion and a blinking between distinct QD charge states.

Surprisingly, the power of the resonant laser impacts the amplitude and dynamics of both processes.

## Device and experimental setup

As schematized in Fig. 1(a), the nanopost optical cavity is built with a segment of photonic wire, which is half-micron-high and features a diameter of 250 nm. This cylindrical structure is made of GaAs, a material with a large refractive index ($n = 3.46$). The nanopost stands on a strongly reflecting planar $SiO_2$-Au mirror[35] while the flat upper facet introduces a weaker top reflection. We focus on a third-order Fabry-Pérot mode that resonates close to $\lambda_c \approx 930$ nm (Fig. 1(b)). Thanks to the ultrasmall volume of the cavity mode ($0.3(\frac{\lambda_c}{n})^3$), a modest quality factor ($Q_c \approx 30$) is sufficient to achieve a large Purcell acceleration ($\times 6$) for an emitter that is located on the first, bottom antinode.[33] This Purcell acceleration is maintained over a bandwith as large as 30 nm at half-maximum. In addition, the strong suppression of the emission into the continuum of free-space modes[36] further enhances the fraction of spontaneous emission coupled to the cavity mode. The nanopost emits a directive output beam, which results from the interference between the upward emission of the top facet and the backscattered part that is reflected by the bottom mirror.[33] For this generation of devices, numerical simulations predict a collection efficiency of 41% into a first lens with a numerical aperture NA = 0.65. Using a larger NA = 0.75 and recent, advanced designs could improve this figure of merit up to 69% (Ref. 34).

Figure 1(c) shows a scanning electron micrograph of a representative device. The nanopost investigated in this work belongs to the same fabrication batch as the one investigated in Ref. 33. The device is 460 nm-high and features a nominal diameter of 250 nm. It embeds a layer of self-assembled InAs QDs ($\sim 5$ QDs per structure on average). Whereas their longitudinal position precisely matches the location of the first antinode (70 nm above the silica layer, see Fig. 1(b)), their lateral location in the wire cross section is random. This does not

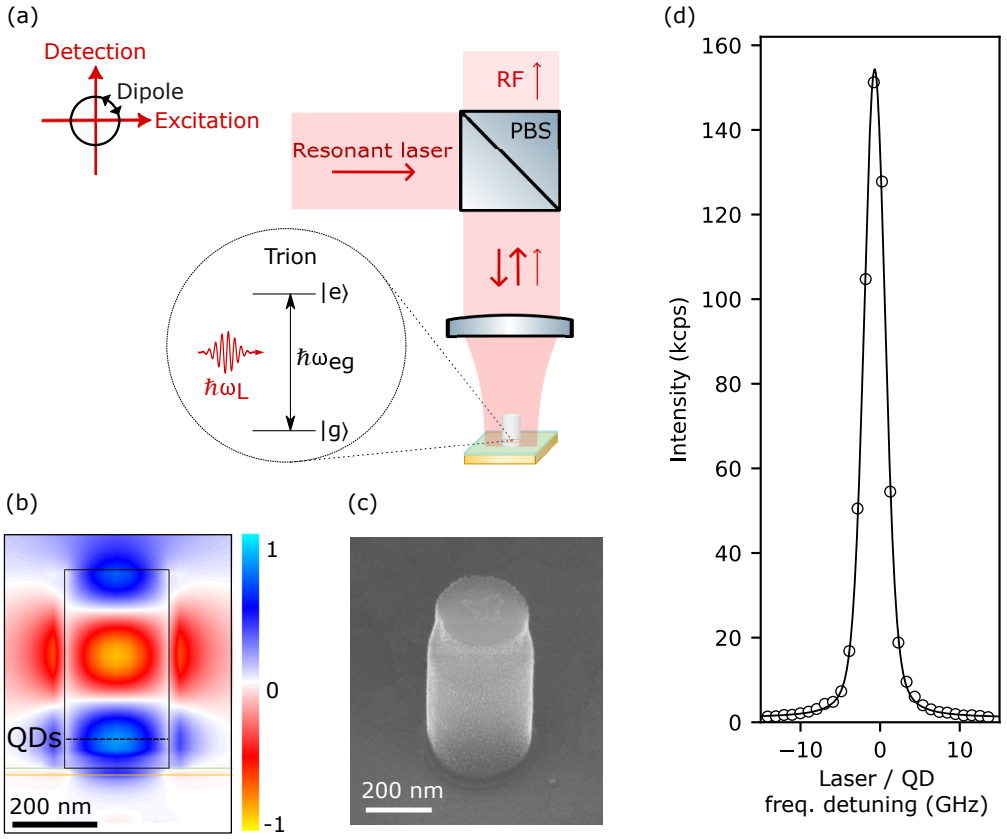


Figure 1: **Resonance fluorescence from a single QD in a nanopost cavity. (a)** Cross-polarized excitation and detection (simplified setup, RF: resonant fluorescence, PBS: polarizing beam splitter). **(b)** Electrical field map for the third-order Fabry-Pérot resonance supported by the nanopost cavity (finite-difference time-domain numerical simulation). The dashed black line indicates the location of the QDs layer, on the first antinode. **(c)** Scanning electron micrograph (tilted view) of a representative device. **(d)** Intensity versus the laser-QD detuning (circles: raw measurement, solid line: fit to a Voigt profile); power of the resonant and non-resonant laser: $P_{\mathrm{L}} = 9\,\mathrm{nW}$ and $P_{\mathrm{nr}} = 160\,\mathrm{nW}$, respectively.

constitute a serious practical limitation: in the presence of spectral and spatial randomness, we indeed estimate that 10% of the emitters feature a Purcell acceleration larger than 50% of the optimal value.[33]

The nanopost device is investigated using a dark-field microscope.[29] As detailed in the SI, the chip is mounted in a liquid-He bath cryostat ($T = 4.2\,\mathrm{K}$). Excitation is provided by a continuous wave tunable diode laser: it features a linewidth below 1 MHz and is frequency- and intensity-stabilized. The laser is focused on the nanopost with an aspheric lens (NA = 0.65), which also collects the resonance fluorescence signal. The latter is detected on

a linear polarization that is orthogonal to the one of the laser. To optimize polarization filtering, we employ polarized beam splitters and a quarter-waveplate to compensate for residual birefringence of the optics, as well as spatial filtering using a single-mode optical fiber.[28] The signal is detected by a pair of superconducting nanowire single-photon detectors forming a Hanbury Brown and Twiss setup. In the following, the signal intensity corresponds to the sum of the detected counts. In correlation mode, the total time jitter of the setup is 35 ps (FWHM).

# Results

We detect the resonance fluorescence of single QDs embedded in a nanopost cavity with a large signal-to-background ratio. We focus here on a trion (singly charged exciton) with an emission wavelength of 936.6 nm. The lifetime of the excited state is $T_1 = 350 \pm 25$ ps, which corresponds to a Purcell acceleration of 4.8 (see SI). Figure 1(d) shows an example linescan: one measures the scattered intensity as the laser frequency $\omega_L/(2\pi)$ is scanned across the QD transition. In this raw experimental trace, the very low background level ($\approx$ 1 kcps) evidences an excellent rejection of stray laser light. We indeed measure a laser rejection by a factor as large as $10^6$. Maintaining this value requires however an excellent stability of the setup. Indeed, a lateral displacement of the nanopost by 10 nm typically decreases the laser rejection by one order of magnitude. With optimal settings, the residual laser light yields a contribution of 60 cps/nW to the background counts.

As observed in other non-gated QD devices,[9,37,38] a weak, non-resonant laser is mandatory to switch-on the resonance fluorescence signal (see SI). This continuous laser is tuned to $\lambda_{nr} = 830$ nm, below the bandgap energy of GaAs, in the absorption continuum associated with the QD wetting layer. The non-resonant laser also excites the luminescence of all the other QDs embedded in the nanopost structure. This contribution is filtered out with a monochromator. Its transmission window is centered on the QD transition of interest and

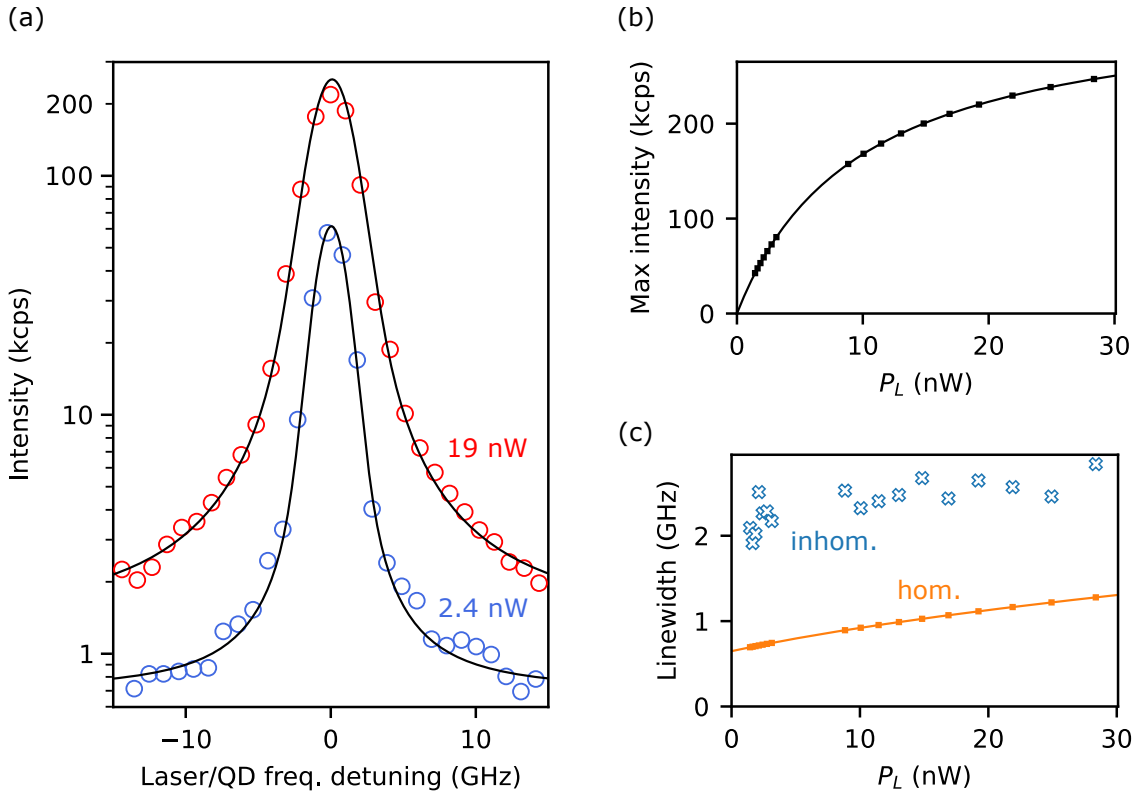


Figure 2: **Power dependence of linescans. (a)** Intensity versus the laser-QD detuning, $(\omega_{\mathrm{L}} - \overline{\omega}_{eg})/(2\pi)$, for two driving powers $P_{\mathrm{L}}$ (circles: raw measurement, solid lines: fit to a Voigt profile (Eq. 1 and model described in the main text)). The intensity scale is logarithmic. **(b)** Predicted power-dependence of the intensity at resonance ($\omega_{\mathrm{L}} = \overline{\omega}_{eg}$). The symbols indicate $P_{\mathrm{L}}$'s for which a linescan was measured. **(c)** Power dependence of the homogeneous and inhomogeneous linewidths ($\Delta\omega_h/(2\pi)$ and $\Delta\omega_i/(2\pi)$, respectively). $\Delta\omega_i/(2\pi) \propto \Sigma$ is a fit parameter. $\Delta\omega_h/(2\pi)$ is computed from the value of the fit parameters $T_2$ and $k$; similarly to panel (b), the symbols indicate $P_{\mathrm{L}}$'s for which a linescan was measured.

features a bandwidth of 50 GHz (200 $\mu$eV). In the following, the non-resonant power is set to $P_{\mathrm{nr}} = 160$ nW. This corresponds to $\sim 2\%$ of the non-resonant saturation power, which yields an additional contribution to the flat background of 700 cps (see SI). Overall, the total background counts are negligible compared to the peak resonance fluorescence signal (signal-to-background ratio $\sim 200:1$).

Figure 2(a) shows two linescans (logarithmic intensity scale), which are measured for an increasing power $P_{\mathrm{L}}$ of the driving laser. In both cases, the experimental data are very well reproduced by a Voigt profile. We further model the QD as a two-level emitter, whose ground state $|g\rangle$ and excited state $|e\rangle$ are separated by an energy $\hbar\omega_{eg}$. The Lorentzian contribution

to the Voigt function is attributed to the homogeneously-broadened emission of the two-level system. The inhomogeneous Gaussian contribution reveals random fluctuations of the QD emission frequency $\omega_{eg}/(2\pi)$, on a time scale that is much longer than the photon emission process. The intensity collected in a linescan experiment then reads:

$$\langle \widetilde{I} \rangle(\omega_{\mathrm{L}}) = b + \eta \mathcal{P}(\mathrm{on}) \int_{-\infty}^{+\infty} \mathrm{d}\omega_{eg} \mathcal{G}(\omega_{eg}) \rho_{ee,s}(\omega_{eg}, \omega_{\mathrm{L}}). \tag{1}$$

The steady-state population of the excited state $|e\rangle$, $\rho_{ee,s}$, accounts for the Lorentzian contribution:

$$\rho_{ee,s} = \frac{S}{2(1+S)} \frac{\Delta\omega_h^2}{4(\omega_{\mathrm{L}} - \omega_{eg})^2 + \Delta\omega_h^2}. \tag{2}$$

Here, $S = \Omega^2 T_1 T_2$ is the saturation parameter, with $\Omega$ the Rabi coupling ($\Omega = k\sqrt{P_{\mathrm{L}}}$, $k$ a proportionality constant), $T_1$ the spontaneous emission time and $T_2$ the total dephasing time; $\Delta\omega_h = 2T_2^{-1}\sqrt{1+S}$ is the homogeneous linewidth (in the angular frequency space). In Eq. 1, $\mathcal{G}(\omega_{eg})$ accounts for the inhomogeneous broadening. This Gaussian probability density is centered at $\overline{\omega}_{eg}$ and features a linewidth $\Delta\omega_i = 2\sqrt{2\ln 2}\Sigma$, with $\Sigma$ the standard deviation. Finally, the prefactor $\mathcal{P}(\mathrm{on})$ is the probability of finding the QD in the charge state of interest; $\eta$ is a global scaling factor and $b$ represents background counts. As discussed later, in addition to linescans, the model also describes intensity autocorrelation measurements; the fit procedure jointly considers these two measurements.

Figure 2(c) shows the homogeneous and inhomogeneous linewidths obtained from this analysis, as a function of the driving power $P_{\mathrm{L}}$. In the low-power limit, the homogeneous linewidth of $\Delta\omega_h/(2\pi) = 650$ MHz is a factor 1.4 above the Fourier limit (the dephasing time, $T_2 = 490$ ps, is equal to $0.70 \times 2T_1$). Still in the low-power limit, the fit yields an inhomogeneous linewidth $\Delta\omega_i/(2\pi) = 2.1$ GHz. The total linewidth amounts to 2.5 GHz, a factor of five above the Fourier transform limit (acquisition time of 1 min).

To gain additional insight over the QD emission dynamics, we measure the intensity autocorrelation function $g^{(2)}(\tau)$ with a Hanbury Brown and Twiss setup. The driving laser

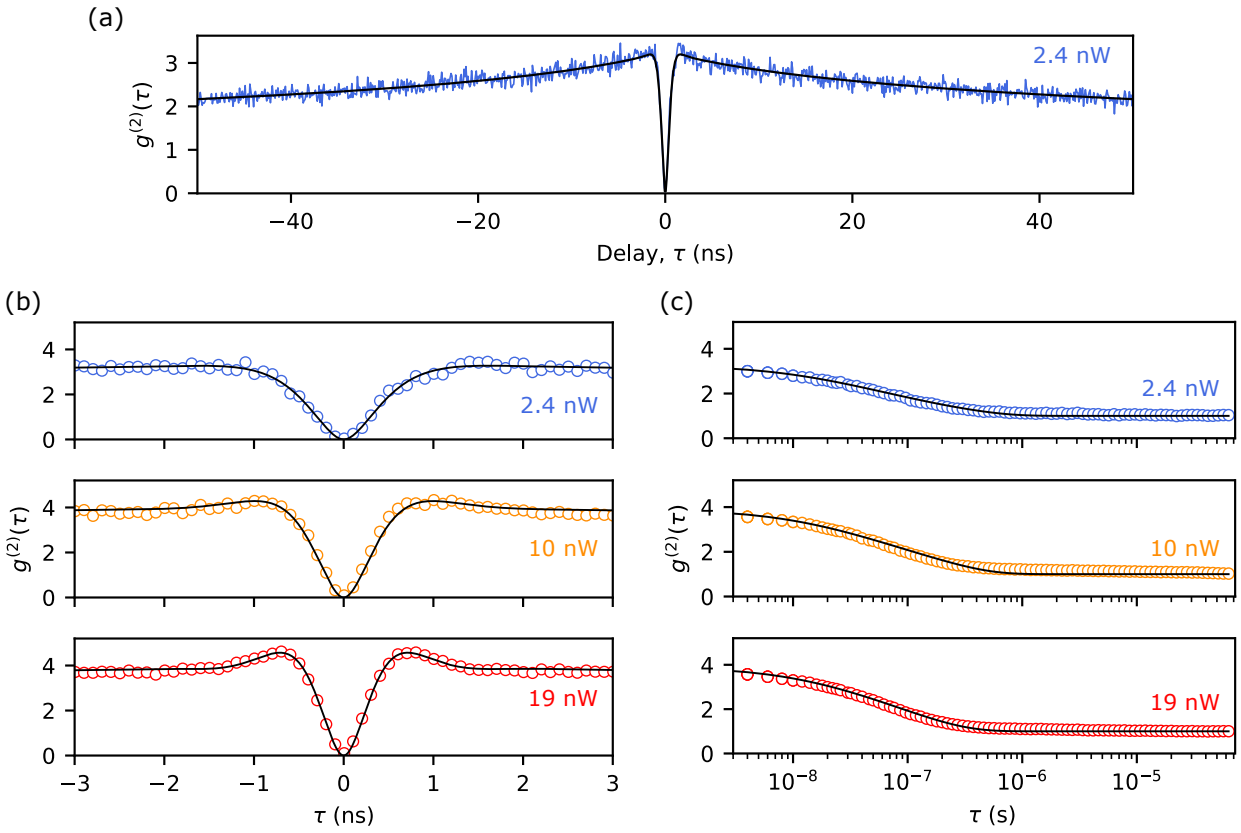


Figure 3: **Intensity autocorrelation.** **(a)** Intensity autocorrelation function for $P_{\mathrm{L}} = 2.4$ nW (blue curve: raw experimental data, black curve: fit to Eq. 3). The data show a clear antibunching at zero delay ($g^{(2)}(0) = 0.02$), and a bunching peak at larger delays ($\max g^{(2)}(\tau) = 3.1$). **(b)** Short delay intensity autocorrelation for 3 different excitation powers (circles: binned raw experimental data (100 ps time bins); dark curve: fit). **(c)** Long delay intensity autocorrelation for the 3 same excitation powers, displayed in a semi-logarithmic scale. The raw experimental data were time-binned logarithmically.

is tuned to the central frequency ($\omega_{\mathrm{L}} = \overline{\omega}_{eg}$). The acquisition time is 2.5 h per experimental trace. Every 20 min, we check and optimize the laser rejection and perform a linescan to track slow drifts of the QD emission frequency.[39] A typical measurement trace is shown in Fig. 3(a). The histogram shows a pronounced dip at zero delay: $g^{(2)}(0)$ is as low as 0.02. On this time scale, the QD behaves as a close-to-ideal two-level system. At larger delays however, the data features a pronounced bunching peak ($g^{(2)}(\tau) \approx 3$). The spectral diffusion process evidenced in the linescans contributes to this bunching peak. Indeed, the random wandering of the QD frequency around the fixed laser frequency results in fluctuations of the emitted intensity. Right after the detection of a first photon, there is a high probability that the

emitter is still close to resonance with the driving laser. The associated bunching amplitude is calculated as $\langle\rho_{ee,s}^2\rangle/\langle\rho_{ee,s}\rangle^2$ (Ref. 20), where $\langle.\rangle$ indicates ensemble averaging over $\omega_{eg}$ using the probability density $\mathcal{G}(\omega_{eg})$ obtained from the fit of linescans. The analysis of the linescan corresponding to Fig. 3(a) yields $\langle\rho_{ee,s}^2\rangle/\langle\rho_{ee,s}\rangle^2 = 1.6$, well below the experimental bunching amplitude. We conclude that another source of bunching is present and consider here a telegraph random blinking.

We now discuss the origin of inhomogeneous broadening and telegraph blinking, starting with the first phenomenon. Inhomogeneous broadening is caused by a slow spectral diffusion process, with a characteristic time well above the motional narrowing limit.[40] An InAs QD in a GaAs nanopost is exposed to several noise sources. First, the QD may experience a random electrical field, due to fluctuations in the occupancy of nearby charge traps. This leads to spectral fluctuations via the quantum-confined Stark effect.[16,40] Second, the QD is also exposed to a magnetic noise, due to fluctuations of nuclear spins.[16] A trion emission line then exhibits a random "breathing" due to the Zeeman effect. The associated spectral broadening has been measured for similar emitters:[16] it is typically one order of magnitude smaller than the value measured in this work. Finally, the QD is also exposed to a random mechanical stress, due to the thermal excitation of the vibration modes of the structure. In a conical microwire, this represents a major source of decoherence.[18,41,42] In a nanopost, the reduced dimensions shift the mechanical resonances to larger frequencies ($\times 10^3$ for the fundamental flexural mode), which dramatically reduces the impact of stress fluctuations. Early estimates using the theoretical framework of Ref. 42 show that the associated spectral broadening is typically 10 times smaller than the experimental linewidth. We conclude that spectral diffusion is here mainly due to electrical noise.

Telegraph blinking is attributed to discrete, random jumps of the QD frequency, on a scale that vastly exceeds the optical linewidth (2.5 GHz). Even though the emitter remains optically active, such large spectral jumps bring the emitter in and out of resonance with the laser, leading in practice to an alternation between bright and dark times. Since linescans

show a single peak over a ±50 GHz span (±200 $\mu$eV), we exclude a spectral shift due to a well-coupled charge trap very close to the QD.[14,15,17] Instead, we consider fluctuations of the charge state of the QD itself, from singly-charged to neutral and vice-versa, which leads to larger spectral shifts.[43] In the following, this process will be refered to as "on/off blinking".

Expanding on recent work,[19,20] we developed an analytical model in order to consistently describe both linescans and intensity autocorrelation measurements. As detailed in the SI, spectral diffusion is modeled by a continuous fluctuation process, which typically arises from the coupling to a large ensemble of identical and independent two-level fluctuators.[20,44] This stationary Markovian process is characterized by the Gaussian probability distribution $\mathcal{G}(\omega_{eg})$ and by the transition probabilities $\mathcal{P}(\omega'_{eg}, t+\tau|\omega_{eg}, t)$. In the latter, the memory of the initial frequency is lost with a characteristic time $\tau_{\mathrm{SD}}$. On/off blinking is modeled as random and discrete jumps between the 'on' and 'off' states, following a Poisson process. The latter is fully characterized by the mean lifetime of the 'on' and 'off' states, $\tau_{\mathrm{on}}$ and $\tau_{\mathrm{off}}$, respectively. They define the stationary probabilities $\mathcal{P}(\mathrm{on}) = \tau_{\mathrm{on}}/(\tau_{\mathrm{on}} + \tau_{\mathrm{off}})$ and $\mathcal{P}(\mathrm{off}) = 1 - \mathcal{P}(\mathrm{on})$, as well as the transition probabilities $\mathcal{P}(j, t+\tau|i, t)$ (with $i, j =$ 'on', 'off'). Here, the memory of the initial state is exponentially lost, with a typical time $\tau_{\mathrm{on/off}} = (\tau_{\mathrm{on}}^{-1} + \tau_{\mathrm{off}}^{-1})^{-1}$. Both on/off blinking and spectral diffusion are supposed to be much slower than the QD photon emission ($\tau_{\mathrm{SD}}, \tau_{\mathrm{on/off}} \gg T_1, T_2$). Furthermore, on/off blinking and spectral diffusion are treated as statistically-independent processes, which enables a factorization of joint probabilities.

In these conditions, the intensity that is collected in a linescan experiment is given by Eq. 1. The intensity autocorrelation function can be factorized as:

$$\widetilde{g}^{(2)}(\tau) = b_{\mathrm{on/off}}(\tau) \times b_{\mathrm{SD}}(\tau) \times \frac{\langle \rho_{ee,s}^2 g^{(2)}(\tau) \rangle}{\langle \rho_{ee,s}^2 \rangle}, \tag{3}$$

with

$$b_{\mathrm{on/off}}(\tau) = 1 + \frac{\tau_{\mathrm{off}}}{\tau_{\mathrm{on}}} e^{-\frac{|\tau|}{\tau_{\mathrm{on/off}}}} \tag{4}$$

$$b_{\mathrm{SD}}(\tau) = \frac{1}{\langle \rho_{ee,s} \rangle^2} \iint \mathrm{d}\omega'_{eg} \mathrm{d}\omega_{eg} \mathcal{P}(\omega'_{eg}, t+\tau | \omega_{eg}, t) \mathcal{G}(\omega_{eg}) \rho_{ee,s}(\omega'_{eg}) \rho_{ee,s}(\omega_{eg}). \tag{5}$$

In Eq. 3, the last factor captures the impact of spectral diffusion on the short-delay dynamics. Here, $g^{(2)}(\tau)$ is the intensity correlation function of an homogeneously-broadened two-level emitter, as obtained from a resolution of the optical Bloch equations in the general, *detuned* case (see *e.g.* Ref. 45). This correction is ruled by the steady-state probability $\mathcal{G}(\omega_{eg})$ and does not depend on the dynamics of spectral diffusion (see SI). Owing to the square dependence on the count rate, this averaging is dominated by quasi-resonant contributions ($\omega_{eg} \approx \omega_{\mathrm{L}}$). Nevertheless, the full expression should be used for an accurate determination of $T_2$. The bunching features due to on/off blinking and spectral diffusion are described by $b_{\mathrm{on/off}}(\tau)$ and $b_{\mathrm{SD}}(\tau)$, respectively. For intermediate delays ($T_1, T_2 \ll |\tau| \ll \tau_{\mathrm{SD}}, \tau_{\mathrm{on/off}}$), the two-level system can be treated as an uncorrelated emitter ($g^{(2)}(\tau) = 1$) while spectral diffusion and on/off blinking are still frozen (in particular $\mathcal{P}(\omega'_{eg}, t+\tau|\omega_{eg}, t) = \delta(\omega'_{eg} - \omega_{eg})$). The total amplitude of the bunching peak is the product $b_{\mathrm{on/off}}(0) \times b_{\mathrm{SD}}(0) = \frac{\tau_{\mathrm{on}}+\tau_{\mathrm{off}}}{\tau_{\mathrm{on}}} \times \frac{\langle \rho_{ee,s}^2 \rangle}{\langle \rho_{ee,s} \rangle^2}$. At larger delays, the decay of the bunching feature is jointly governed by the dynamics of on/off blinking and spectral diffusion.

This simple model faithfully reproduces the complete experimental dataset: linescans (Fig. 2) and intensity autocorrelation (Fig. 3) for various laser powers (16 values of $P_{\mathrm{L}}$ in the range of 1.8 nW − 28 nW). The fit parameters $T_2 = 490$ ps and $k = \Omega/\sqrt{P_{\mathrm{L}}} = 2\pi \times 122\ \mathrm{MHz}/\sqrt{\mathrm{nW}}$ are common to the complete data set, whereas the parameters of spectral diffusion ($\Sigma$ and $\tau_{\mathrm{SD}}$) and on/off blinking ($\tau_{\mathrm{on}}$ and $\tau_{\mathrm{off}}$) are adjusted for each laser power. The complete fit procedure is detailed in the SI. Importantly, the homogeneous and inhomogeneous contributions to spectral broadening can be further disentangled thanks to the time resolution of $g^{(2)}$-measurements. Indeed, the short-delay dip is mostly sensitive to

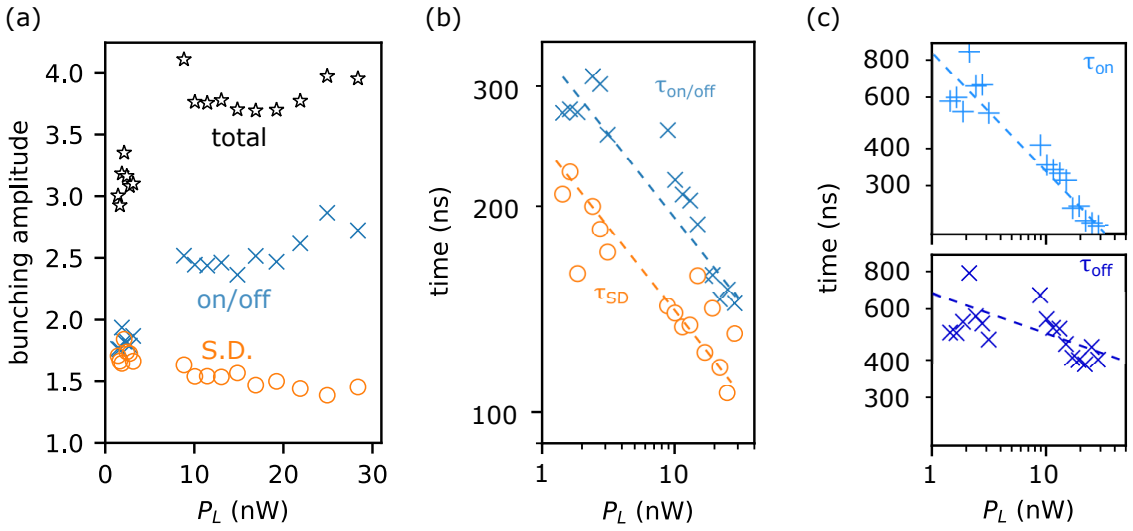


Figure 4: **Characterization of spectral diffusion and on/off blinking. (a)** Bunching amplitudes as a function of the excitation power $P_L$: total bunching amplitude (black stars), contribution of spectral diffusion (orange circles), and contribution of on/off blinking (blue crosses). **(b)** Characteristic time of the spectral diffusion ($\tau_{\mathrm{SD}}$, orange circles) and of the on/off blinking ($\tau_{\mathrm{on/off}}$, blue crosses) versus $P_{\mathrm{L}}$. The dashed lines are fits to an empirical power law $\propto P_{\mathrm{L}}^{\alpha}$, which yields $\alpha = -0.25$. **(c)** Lifetime of the "on" state ($\tau_{\mathrm{on}}$, top panel) and of the "off" state ($\tau_{\mathrm{off}}$, bottom panel) versus $P_{\mathrm{L}}$, plotted in a log/log scale. The dashed lines are a fit to a power law (top panel: $\alpha = -0.4$, bottom panel: $\alpha = -0.1$).

$T_2$ and $\Omega$ (homogeneous contributions), whereas the bunching peak observed at longer delays is in particular sensitive to $\Sigma$ (inhomogeneous contribution). Overall, this method enables an extensive characterization of the QD emission (dephasing, spectral fluctuations, on/off blinking), over a broad range of timescales.

We now focus on spectral diffusion. Figure 4(a) reveals that the associated bunching amplitude, $\frac{\langle \rho_{ee,s}^2 \rangle}{\langle \rho_{ee,s} \rangle^2}$, decreases when the laser power $P_{\mathrm{L}}$ increases. This is expected: the ratio $\Delta\omega_h/\Delta\omega_i$ increases with $P_{\mathrm{L}}$ due to power broadening (Fig. 2(c)). Therefore, at large driving powers, the QD has a higher probability to remain close-to-resonance with the laser, resulting in a decrease in the intensity fluctuations. Figure 4(b) shows that spectral diffusion is a fast process ($\tau_{\mathrm{SD}} \sim 200$ ns in the low-power limit). High-frequency electrical noise can be generated by non-resonant excitation[16] and has also been observed in QDs embedded in bottom-up nanowires.[46] Unexpectedly, the dynamics of spectral diffusion depends on the power of the resonant laser: $\tau_{\mathrm{SD}}$ decreases as $P_{\mathrm{L}}$ increases, following the empirical power law

$\tau_{SD} \propto P_L^{-0.25}$.

Figure 4(a) shows that the on/off bunching amplitude, $\frac{\tau_{on}+\tau_{off}}{\tau_{on}} = \frac{1}{\mathcal{P}(on)}$, strongly increases with the laser power. At low powers, spectral diffusion and on/off blinking feature similar bunching amplitudes. At large powers ($\geq$ 10nW), the contribution of on/off blinking becomes dominant. We note that it is mandatory to take this feature into account for a correct description of the saturation of the linescan intensity (Fig. 2(b)). Figure 4(b) shows the characteristic time $\tau_{on/off}$ as a function of the laser power. Starting from a low-power value of 300 ns, $\tau_{on/off}$ decreases with $P_L$, with a similar power law that $\tau_{SD}$. This variation is mainly due to the pronounced decrease of $\tau_{on}$ (see Fig. 4(c)).

# Discussion and outlook

Taken together, these results show that the resonant laser either modifies the charge dynamics in the QD environment and/or creates additional charges. At first sight, the excitation of charges with a laser having a photon energy well-below the bandgap energy of the QD wetting layer seems rather surprising. However such a process has been reported for similar QDs embedded in a micropillar cavity.[17] In a conical photonic wire, significant subgap optical absorption, close to the QD transition energy, was revealed through the observation of photothermal forces.[31] Surfaces hosting uncontrolled electronic states may play a role here. We also note that the charge loading and unloading in the QD may result from complex microscopic processes (see *e.g.* Ref. 37). Whereas the power dependencies obtained in this work will certainly guide microscopic modeling, additional, future research is necessary to elucidate this intriguing phenomenology.

Both the excellent anti-bunching and the dephasing time close to the Fourier limit are promising for the emission of indistinguishable single photons. Thanks to the Purcell effect, the ratio $I = T_2/(2T_1)$ reaches 0.70 for a QD in a nanopost. This represents a significant improvement over photonic wire antennas, obtained either with a top-down approach ($I =$

0.28, Ref. 47) or with a bottom-up one ($I = 0.37$ and 0.5, Refs. 48 and 49, respectively). Remarkably, these two latter results were obtained under non-resonant optical excitation, leaving room for future improvements with a strictly resonant excitation. Practical, on-demand operation of the source requires a pulsed excitation scheme. Very recently, clean polarization filtering was demonstrated for the pulsed resonant excitation of a QD in a tapered bottom-up wire.[32]

To tame residual charge noise, future nanopost devices will include an electrostatic gate.[16,50] This suppresses slow spectral diffusion and stabilizes the charge state of the QD. *p-i-n* structures have been successfully implemented in suspended waveguides with lateral dimensions similar to the ones of the nanopost, leading to the emission of highly coherent photons.[11,51] In practice, the top contact could be obtained with a thin, suspended membrane made of a transparent oxyde. On the photonic side, moving the QD to the second antinode of the Fabry-Pérot mode will improve the Purcell acceleration.[34] This will also bring the QD farther from the anchoring, thus reducing the coupling to the fundamental flexural mode, a residual source of thermomechanical decoherence.

Beyond quantum photonics, this work also opens promising perspectives for QD-nanowire hybrid nanomechanics. When the mechanical resonance frequency exceeds the emitter linewidth, spectrally-resolved Raman sidebands appear in the spectrum of the coupled system.[39,52–54] In analogy with trapped-ion systems, a selective optical excitation of these sidebands allows cooling down the resonator to its ground state,[55] and, ultimately, generating quantum state of motion. Towards this ambitious goal, both the detection of resonance fluorescence from a QD in a nanopost and the narrow spectral linewidth of the emitter are important technical achievements. Compared to earlier work with conical microwires,[31,56,57] the low mass of the nanopost brings the first vibration modes in the GHz range and increases the coupling strength.

## Conclusions

To conclude, we demonstrated resonance fluorescence from a single QD embedded in a nanopost cavity. Thanks to a cross-polarization scheme, we achieve a large signal-to-background ratio. By combining linescans and intensity auto-correlation measurements, jointly discribed by an analytical model, we extensively characterized the QD emission dynamics. Despite the proximity of surfaces, the emitter shows appealing performance, with moderate noise levels. With future device improvements, the broadband nanopost cavity thus constitutes a promising building block for the realization of bright and widely tunable sources of indistinguishable single photons.

## Acknowledgement

The authors acknowledge fruitful discussions with Joël Bleuse, Aymeric Delteil, Jean-Pierre Hermier, Jacek Kasprzack, Olivier Krebs, Loïc Lanco and Mathieu Munsch. This work was supported by: the French Agence Nationale de la Recherche (ANR) IPOD grant (No. ANR-19-CE47-0009-02), the ANR France 2030 grant OQULUS (No. ANR-23-PETQ-013), the QUANTERA grant FIGANTI (No. ANR-24-QUA2-0001), the European Union's Horizon 2020 research and innovation program under the Marie Skłodowska-Curie Grant Agreement QUDOT-TECH (No. 861097), the European Research Council (project UNITY, grant No. 865230) and the Swiss National Science Foundation (Project No. 200020_204069). Sample fabrication was carried out in the Grenoble Upstream Nanofabrication Facility (PTA).

## Supporting Information

See Supporting Information for: i) the description of the experimental setup and the measurement process, ii) the analytical model, iii) the fit procedure, iv) the impact of the non-resonant laser, v) the contributions to the background counts, vi) the quantification of the

Purcell acceleration.

## Data availability

The data that support the findings of this study are available from the corresponding author upon reasonable request.

## References


(1) Flagg, E. B.; Muller, A.; Robertson, J. W.; Founta, S.; Deppe, D. G.; Xiao, M.; Ma, W.; Salamo, G. J.; Shih, C. K. Resonantly driven coherent oscillations in a solid-state quantum emitter. Nat. Phys. **2009**, 5, 203–207.

(2) Nguyen, H. S.; Sallen, G.; Voisin, C.; Roussignol, P.; Diederichs, C.; Cassabois, G. Ultra-coherent single photon source. Appl. Phys. Lett. **2011**, 99, 261904.

(3) Ulhaq, A.; Weiler, S.; Ulrich, S. M.; Roßbach, R.; Jetter, M.; Michler, P. Cascaded single-photon emission from the Mollow triplet sidebands of a quantum dot. Nature Photon. **2012**, 6, 238–242.

(4) Matthiesen, C.; Vamivakas, A. N.; Atatüre, M. Subnatural linewidth single photons from a quantum dot. Phys. Rev. Lett. **2012**, 108, 093602.

(5) Schulte, C. H. H.; Hansom, J.; Jones, A. E.; Matthiesen, C.; Le Gall, C.; Atatüre, M. Quadrature squeezed photons from a two-level system. Nature **2015**, 525, 222–225.

(6) Phillips, C. L.; Brash, A. J.; McCutcheon, D. P. S.; Iles-Smith, J.; Clarke, E.; Royall, B.; Skolnick, M. S.; Fox, A. M.; Nazir, A. Photon Statistics of Filtered Resonance Fluorescence. Phys. Rev. Lett. **2020**, 125, 043603.

(7) Hanschke, L. et al. Origin of Antibunching in Resonance Fluorescence. Phys. Rev. Lett. **2020**, 125, 170402.

(8) Heindel, T.; Kim, J.-H.; Gregersen, N.; Rastelli, A.; Reitzenstein, S. Quantum dots for photonic quantum information technology. Adv. Opt. Photon. **2023**, 15, 613–738.

(9) Nguyen, H. S.; Sallen, G.; Voisin, C.; Roussignol, P.; Diederichs, C.; Cassabois, G. Optically Gated Resonant Emission of Single Quantum Dots. Phys. Rev. Lett. **2012**, 108, 057401.

(10) Kuhlmann, A. V.; Prechtel, J. H.; Houel, J.; Ludwig, A.; Reuter, D.; Wieck, A. D.; Warburton, R. J. Transform-limited single photons from a single quantum dot. Nat. Commun. **2015**, 6, 8204.

(11) Thyrrestrup, H. et al. Quantum Optics with Near-Lifetime-Limited Quantum-Dot Transitions in a Nanophotonic Waveguide. Nano Lett. **2018**, 18, 1801–1806.

(12) Somaschi, N. et al. Near-optimal single-photon sources in the solid state. Nature Photon. **2016**, 10, 340–345.

(13) Ding, X.; He, Y.; Duan, Z.-C.; Gregersen, N.; Chen, M.-C.; Unsleber, S.; Maier, S.; Schneider, C.; Kamp, M.; Höfling, S.; Lu, C.-Y.; Pan, J.-W. On-Demand Single Photons with High Extraction Efficiency and Near-Unity Indistinguishability from a Resonantly Driven Quantum Dot in a Micropillar. Phys. Rev. Lett. **2016**, 116, 020401.

(14) Vamivakas, A. N.; Zhao, Y.; Fält, S.; Badolato, A.; Taylor, J. M.; Atatüre, M. Nanoscale Optical Electrometer. Phys. Rev. Lett. **2011**, 107, 166802.

(15) Houel, J.; Kuhlmann, A. V.; Greuter, L.; Xue, F.; Poggio, M.; Gerardot, B. D.; Dalgarno, P. A.; Badolato, A.; Petroff, P. M.; Ludwig, A.; Reuter, D.; Wieck, A. D.; Warburton, R. J. Probing Single-Charge Fluctuations at a GaAs/AlAs Interface Using Laser Spectroscopy on a Nearby InGaAs Quantum Dot. Phys. Rev. Lett. **2012**, 108, 107401.

(16) Kuhlmann, A. V.; Houel, J.; Ludwig, A.; Greuter, L.; Reuter, D.; Wieck, A. D.; Poggio, M.; Warburton, R. J. Charge noise and spin noise in a semiconductor quantum device. Nature Phys. **2013**, 9, 570–575.

(17) Arnold, C.; Loo, V.; Lemaître, A.; Sagnes, I.; Krebs, O.; Voisin, P.; Senellart, P.; Lanco, L. Cavity-Enhanced Real-Time Monitoring of Single-Charge Jumps at the Microsecond Time Scale. Phys. Rev. X **2014**, 4, 021004.

(18) Munsch, M.; Kuhlmann, A. V.; Cadeddu, D.; Gérard, J.-M.; Claudon, J.; Poggio, M.; Warburton, R. J. Resonant driving of a single photon emitter embedded in a mechanical oscillator. Nat. Commun. **2017**, 8, 76.

(19) Fournier, C.; Watanabe, K.; Taniguchi, T.; Barjon, J.; Buil, S.; Hermier, J.-P.; Delteil, A. Investigating the fast spectral diffusion of a quantum emitter in hBN using resonant excitation and photon correlations. Phys. Rev. B **2023**, 107, 195304.

(20) Delteil, A.; Buil, S.; Hermier, J.-P. Photon statistics of resonantly driven spectrally diffusive quantum emitters. Phys. Rev. B **2024**, 109, 155308.

(21) Uppu, R.; Eriksen, H. T.; Thyrrestrup, A. D., H. ans Uğurlu; Wang, Y.; Scholz, S.; Wieck, A. D.; Ludwig, A.; Löbl, M. C.; Warburton, R. J.; Lodahl, P.; Midolo, L. On-chip deterministic operation of quantum dots in dual-mode waveguides for a plug-and-play single-photon source. Nat. Commun. **2020**, 11, 3782.

(22) Muller, A.; Flagg, E. B.; Bianucci, P.; Wang, X. Y.; Deppe, D. G.; Ma, W.; Zhang, J.; Salamo, G. J.; Xiao, M.; Shih, C. K. Resonance Fluorescence from a Coherently Driven Semiconductor Quantum Dot in a Cavity. Phys. Rev. Lett. **2007**, 99, 187402.

(23) Makhonin, M. N.; Dixon, J. E.; Coles, R. J.; Royall, B.; Clarke, E.; Skolnick, M. S.; Fox, A. M. Waveguide Coupled Resonance Fluorescence from On-Chip Quantum Emitter. Nano Lett. **2014**, 14, 6997–7002.

(24) Reigue, A.; Iles-Smith, J.; Lux, F.; Monniello, L.; Bernard, M.; Margaillan, F.; Lemaitre, A.; Martinez, A.; McCutcheon, D. P. S.; Mørk, J.; Hostein, R.; Voliotis, V. Probing Electron-Phonon Interaction through Two-Photon Interference in Resonantly Driven Semiconductor Quantum Dots. Phys. Rev. Lett. **2017**, 118, 233602.

(25) Englund, D.; Majumdar, A.; Faraon, A.; Toishi, M.; Stoltz, N.; Petroff, P.; Vučović, J. Resonant Excitation of a Quantum Dot Strongly Coupled to a Photonic Crystal Nanocavity. Phys. Rev. Lett. **2010**, 104, 073904.

(26) Reinhard, A.; Volz, T.; Winger, M.; Badolato, A.; Hennessy, K. J.; Hu, E. L.; Imamoğlu, A. Strongly correlated photons on a chip. Nature Photon. **2011**, 6, 93–96.

(27) Leandro, L.; Hastrup, J.; Reznik, R.; Cirlin, G.; Akopian, N. Resonant excitation of nanowire quantum dots. npj Quantum Inf. **2020**, 6, 93.

(28) Benelajla, M.; Kammann, E.; Urbaszek, B.; Karrai, K. Physical Origins of Extreme Cross-Polarization Extinction in Confocal Microscopy. Phys. Rev. X **2021**, 11, 021007.

(29) Kuhlmann, A. V.; Houel, J.; Brunner, D.; Ludwig, A.; Reuter, D.; Wieck, A. D.; Warburton, R. J. A dark-field microscope for background-free detection of resonance fluorescence from single semiconductor quantum dots operating in a set-and-forget mode. Rev. Sci. Instrum. **2013**, 84, 073905.

(30) Tomm, N.; Javadi, A.; Antoniadis, N. O.; Najer, D.; Löbl, M. C.; Korsch, A. R.; Schott, R.; Valentin, S. R.; Wieck, A. D.; Ludwig, A.; Warburton, R. J. A bright and fast source of coherent single photons. Nat. Nanotechnol. **2021**, 16, 399–403.

(31) Kettler, J.; Vaish, N.; Mercier de Lépinay, L.; Besga, B.; de Assis, P.-L.; Bourgeois, O.; Auffèves, A.; Richard, M.; Claudon, J.; Gérard, J.-M.; Pigeau, B.; Arcizet, O.; Verlot, P.; Poizat, J.-P. Inducing micromechanical motion by optical excitation of a single quantum dot. Nat. Nanotechnol. **2021**, 16, 283–287.

(32) Gao, J.; Krishna, G.; Yeung, E.; Yu, L.; Gangopadhyay, S.; Chan, K.-S.; Huang, C.-T.; Descamps, T.; Reimer, M. E.; Poole, P. J.; Dalacu, D.; Zwiller, V.; Elshaari, A. W. On demand single photon generation and coherent control of excitons from resonantly driven nanowire quantum dots. 2024-09-23; `https://arxiv.org/abs/2409.14964`.

(33) Kotal, S.; Artioli, A.; Wang, Y.; Osterkryger, A. D.; Finazzer, M.; Fons, R.; Genuist, Y.; Bleuse, J.; Gérard, J.-M.; Gregersen, N.; Claudon, J. A nanowire optical nanocavity for broadband enhancement of spontaneous emission. Appl. Phys. Lett. **2021**, 118, 194002.

(34) Jacobsen, M. A.; Wang, Y.; Vannucci, L.; Claudon, J.; Gérard, J. M.; Gregersen, N. Performance of the nanopost single-photon source: beyond the single-mode model. Nanoscale **2023**, 15, 6156–6169.

(35) Friedler, I.; Lalanne, P.; Hugonin, J. P.; Claudon, J.; Gérard, J. M.; Beveratos, A.; Robert-Philip, I. Efficient photonic mirrors for semiconductor nanowires. Opt. Lett. **2008**, 33, 2635–2637.

(36) Bleuse, J.; Claudon, J.; Creasey, M.; Malik, N. S.; Gérard, J.-M.; Maksymov, I.; Hugonin, J.-P.; Lalanne, P. Inhibition, Enhancement, and Control of Spontaneous Emission in Photonic Nanowires. Phys. Rev. Lett. **2011**, 106, 103601.

(37) Nguyen, H. S.; Sallen, G.; Abbarchi, M.; Ferreira, R.; Voisin, C.; Roussignol, P.; Cassabois, G.; Diederichs, C. Photoneutralization and slow capture of carriers in quantum dots probed by resonant excitation spectroscopy. Phys. Rev. B **2013**, 87, 115305.

(38) Jahn, J.-P.; Munsch, M.; Béguin, L.; Kuhlmann, A. V.; Renggli, M.; Huo, Y.; Ding, F.; Trotta, R.; Reindl, M.; Schmidt, O. G.; Rastelli, A.; Treutlein, P.; Warburton, R. J. An artificial Rb atom in a semiconductor with lifetime-limited linewidth. Phys. Rev. B **2015**, 92, 245439.

(39) Spinnler, C.; Nguyen, G. N.; Wang, Y.; Zhai, L.; Javadi, A.; Erbe, M.; Scholz, S.; Wieck, A. D.; Ludwig, A.; Lodahl, P.; Midolo, L.; Warburton, R. J. A single-photon

emitter coupled to a phononic-crystal resonator in the resolved-sideband regime. Nature Commun **2024**, 15, 9509.

(40) Berthelot, A.; Favero, I.; Cassabois, G.; Voisin, C.; Delalande, C.; Roussignol, P.; Ferreira, R.; Gérard, J. M. Unconventional motional narrowing in the optical spectrum of a semiconductor quantum dot. Nature Phys. **2006**, 2, 759–764.

(41) Tighineanu, P.; Dreeßen, C. L.; Flindt, C.; Lodahl, P.; Sørensen, A. S. Phonon Decoherence of Quantum Dots in Photonic Structures: Broadening of the Zero-Phonon Line and the Role of Dimensionality. Phys. Rev. Lett. **2018**, 120, 257401.

(42) Artioli, A.; Kotal, S.; Gregersen, N.; Verlot, P.; Gérard, J.-M.; Claudon, J. Design of Quantum Dot-Nanowire Single-Photon Sources that are Immune to Thermomechanical Decoherence. Phys. Rev. Lett. **2019**, 123, 247403.

(43) Dalgarno, P. A.; Smith, J. M.; McFarlane, J.; Gerardot, B. D.; K., K.; Badolato, A.; Petroff, P. M.; Warburton, R. J. Coulomb interactions in single charged self-assembled quantum dots: Radiative lifetime and recombination energy. Phys. Rev. B **2008**, 77, 245311.

(44) Berthelot, A.; Voisin, C.; Delalande, C.; Roussignol, P.; Ferreira, R.; Cassabois, G. From random telegraph to Gaussian stochastic noises: Decoherence and spectral diffusion in a semiconductor quantum dot. Adv. Math. Phys. **2010**, 2010, 494738.

(45) Noh, H.-R.; Jhe, W. Analytic solutions of the optical Bloch equations. Optics Communications **2010**, 283, 2353–2355.

(46) Sallen, G.; Tribu, A.; Aichele, T.; André, R.; Besombes, L.; Bougerol, C.; Richard, M.; Tatarenko, S.; Kheng, K.; Poizat, J.-P. Subnanosecond spectral diffusion measurement using photon correlation. Nature Photon. **2010**, 4, 696–699.

(47) Mermillod, Q.; Jakubczyk, T.; Delmonte, V.; Delga, A.; Peinke, E.; Gérard, J.-M.; Claudon, J.; Kasprzak, J. Harvesting, Coupling, and Control of Single-Exciton Coherences in Photonic Waveguide Antennas. Phys. Rev. Lett. **2016**, 116, 163903.

(48) Reimer, M. E.; Bulgarini, G.; Fognini, A.; Heeres, R. W.; Witek, B. J.; Versteegh, M. A. M.; Rubino, A.; Braun, T.; Kamp, M.; Höfling, S.; Dalacu, D.; Lapointe, J.; Poole, P. J.; Zwiller, V. Overcoming power broadening of the quantum dot emission in a pure wurtzite nanowire. Phys. Rev. B **2016**, 93, 195316.

(49) Laferrière, P.; Yin, A.; Yeung, E.; Kusmic, L.; Korkusinski, M.; Rasekh, P.; Northeast, D. B.; Haffouz, S.; Lapointe, J.; Poole, P. J.; Williams, R. L.; Dalacu, D. Approaching transform-limited photons from nanowire quantum dots using excitation above the band gap. Phys. Rev. B **2023**, 107, 155422.

(50) Zhai, L.; Löbl, M. C.; Nguyen, G. N.; Ritzmann, J.; Javadi, A.; Spinnler, C.; Wieck, A. D.; Ludwig, A.; Warburton, R. J. Low-noise GaAs quantum dots for quantum photonics. Nature Commun. **2020**, 11, 4745.

(51) Grim, J. Q.; Bracker, A. S.; Zalalutdinov, M.; Carter, S. G.; Kozen, A. C.; Kim, M.; Kim, C. S.; Mlack, J. T.; Yakes, M.; Lee, B.; Gammon, D. Scalable in operando strain tuning in nanophotonic waveguides enabling three-quantum-dot superradiance. Nat. Mater. **2019**, 18, 963–969.

(52) Weiß, M.; Wigger, D.; Nägele, M.; Müller, K.; Finley, J. J.; Kuhn, T.; Machnikowski, P.; Krenner, H. J. Optomechanical wave mixing by a single quantum dot. Optica **2021**, 8, 291–300.

(53) Spinnler, C.; Nguyen, G. N.; Wang, Y.; Erbe, M.; Javadi, A.; Zhai, L.; Scholz, S.; Wieck, A. D.; Ludwig, A.; Lodahl, P.; Midolo, L.; Warburton, R. J. Quantum dot coupled to a suspended-beam mechanical resonator: From the unresolved- to the resolved-sideband regime. Phys. Rev. Appl. **2024**, 21, 034046.

(54) DeCrescent, R. A.; Wang, Z.; Bush, J. T.; Imany, P.; Kwiatkowski, A.; Reddy, D. V.; Nam, S. W.; Mirin, R. P.; Silverman, K. L. Coherent dynamics in an optical quantum dot with phonons and photons. Optica **2024**, 11, 1526–1532.

(55) Wilson-Rae, I.; Zoller, P.; Imamoğlu, A. Laser Cooling of a Nanomechanical Resonator Mode to its Quantum Ground State. Phys. Rev. Lett. **2004**, 92, 075507.

(56) Yeo, I.; de Assis, P.-L.; Gloppe, A.; Dupont-Ferrier, E.; Verlot, P.; Malik, N. S.; Dupuy, E.; Claudon, J.; Gérard, J.-M.; Auffèves, A.; Nogues, G.; Seidelin, S.; Poizat, J.-P.; Arcizet, O.; Richard, M. Strain-mediated coupling in a quantum dot-mechanical oscillator hybrid system. Nature Nanotech. **2014**, 9, 106–110.

(57) Tanos, R.; Tlili, H.; Curé, Y.; Finazzer, M.; Artioli, A.; Kotal, S.; Genuist, Y.; Verlot, P.; Bleuse, J.; Gérard, J.-M.; Claudon, J. High-Order Nanowire Resonances for High-Frequency, Large-Coupling-Strength Quantum Dot Hybrid Nanomechanics. ACS Photonics **2024**, 11, 1352–1358.

# TOC Graphic

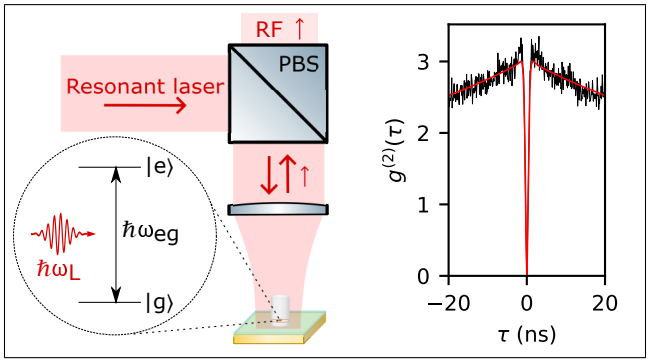

# Supporting Information: Resonance fluorescence from a single quantum dot in a nanopost optical cavity

Maxime Gaignard,[†,‖] Matteo Finazzer,[†,‖] Clemens Spinnler,[‡] Giang N. Nguyen,[‡] Saptarshi Kotal,[†] Alberto Artioli,[†] Yann Genuist,[¶] Niels Gregersen,[§] Jean-Philippe Poizat,[¶] Jean-Michel Gérard,[†] Richard J. Warburton,[‡] and Julien Claudon[*,†]

†*Univ. Grenoble Alpes, CEA, Grenoble INP, IRIG, PHELIQS, "Nanophysique et semiconducteurs" group, F-38000 Grenoble, France*

‡*Department of Physics, University of Basel, Klingelbergstrasse 82, CH-4056 Basel, Switzerland*

¶*Univ. Grenoble Alpes, CNRS, Grenoble INP, Institut Néel, "Nanophysique et semiconducteurs" group, F-38000 Grenoble, France*

§*DTU Electro, Department of Electrical and Photonics Engineering, 2800 Kongens Lyngby, Denmark*

‖*M.G. and M.F. contributed equally to this work*

E-mail: julien.claudon@cea.fr

# Contents

# 1 Experimental details

## 1.1 Setup

Resonance fluorescence (RF) is measured with a dark-field microscope, very close to the one described in Ref. S1. For all experiments presented in this article, the QD was excited using a resonant CW laser, plus a weak non-resonant laser. The emission wavelength of the "resonant" laser (Toptica DL pro) is tunable, and is stabilized using a wavemeter and a feedback loop controlling the laser cavity piezo actuators. A double-pass AOM setup stabilizes the laser power. The laser control and monitoring setup is detailed in Fig. S2.

The auxiliary non-resonant excitation was performed using a laser diode emitting at 830 nm. The associated photon energy is below the bandgap of GaAs, in the 2D absorption continuum of the QDs wetting layer. In the measurements discussed in the main text, the non-resonant power is set to 160 nW ($\sim$ 2% of the non-resonant saturation power). The non-resonant power is not stabilized, but the relative power variations are estimated to be smaller than 5%.

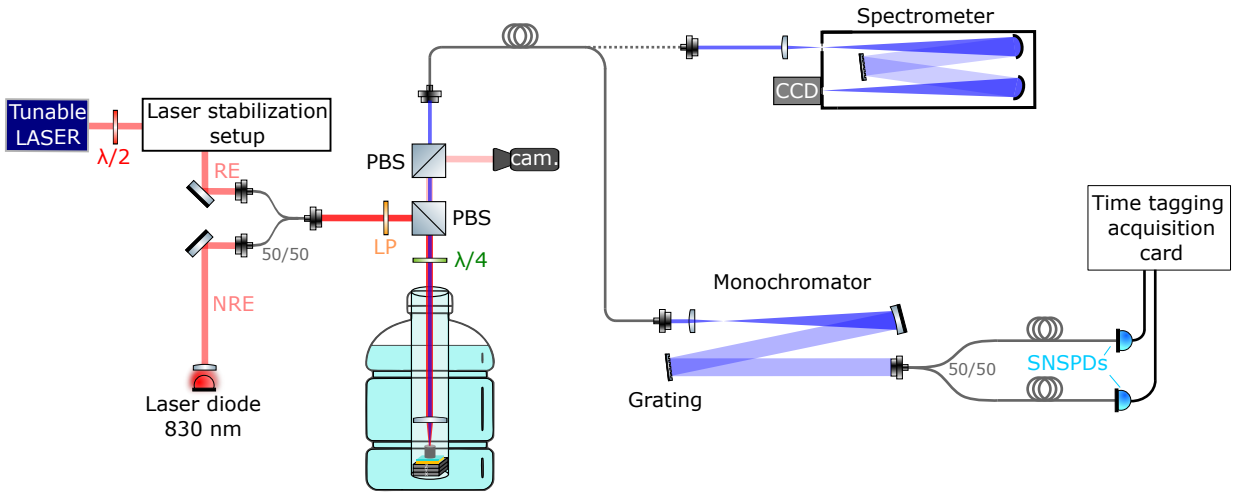


Figure S1: **Experimental setup.** "50/50": 50:50 fibered beamsplitter; "RE": Resonant excitation; "NRE": Non-resonant excitation; "$\lambda/2$": Half-wave plate; "$\lambda/4$": Quarter-wave plate; "PBS": Polarizing beam splitter; "Cam.": Infrared camera; "CCD": Charge coupled device camera; "SNSPDs": Superconducting nanowire single-photon detectors.

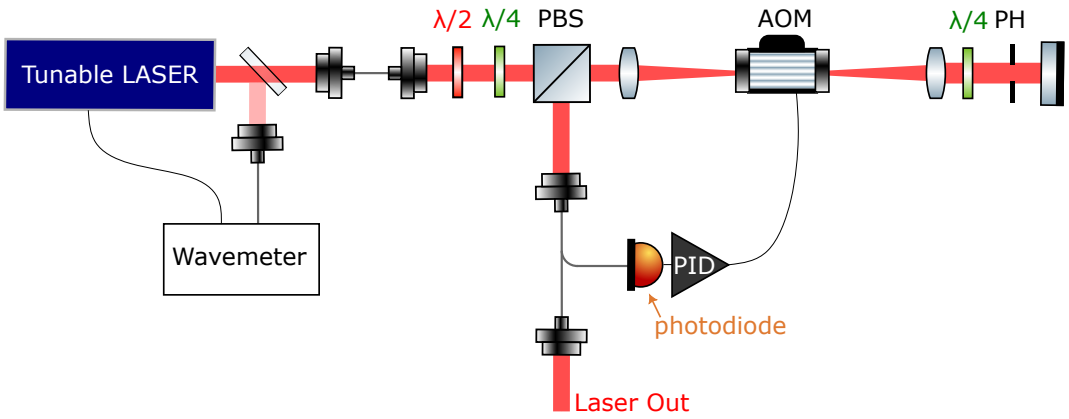


Figure S2: **Laser stabilization setup.**"$\lambda/2$": Halfwave plate; "$\lambda/4$": Quarterwave plate; "PBS": Polarizing beamsplitter; "PH": Pinhole; "AOM": Acousto-optic modulator; "PID": Proportional–integral–derivative controller.

The nanopost device is placed in a vacuum tube that is immersed in a liquid helium bath cryostat. The tube is filled with helium gas, providing good thermalization with the helium bath ($T = 4.2\,\mathrm{K}$). The gas reaches a pressure of $10^{-3}\,\mathrm{mbar}$ at $4\,\mathrm{K}$. The sample is mounted on a stage whose position is controlled by a set of 3 piezo steppers ($10\,\mathrm{nm}$ positioning accuracy). An aspheric lens (numerical aperture of 0.65) focuses the excitation laser on the sample and collects the QD resonance fluorescence.

In order to separate the QD RF signal from reflected and stray laser light, we employ a cross-polarized scheme for the excitation and the detection. The laser is vertically polarized. It excites the QD dipoles (for a trion with no magnetic field: two circular dipoles with clockwise and counter-clockwise orientations). The laser is filtered using a pair of polarizing beam splitters (PBS), whereas the QD RF is half-transmitted towards the detectors. A linear polarizer ensures excellent control over the laser polarization. In addition, a quarter-wave plate, placed between the cryostat window and the pair of PBS, compensates for the birefringence phenomena induced by the optics. High-precision rotation stages allow for an excellent control of the waveplates and polarizer angles ($\leq 3.6$ arcsec) which is mandatory to reach a good laser rejection. Due to the reflection of the laser on a strongly focused spot, the polarization of high-order modes is perturbed,[S2] and therefore they are not strongly rejected by the PBS pair. Therefore, the RF signal is collected by a single-mode fiber (with

an 80% collection efficiency) which allows to select only the $TEM_{00}$ spatial mode and reject other modes. The complete setup provides laser extinction ratio as large as $10^6$, the latter being strongly dependant on the position of the focused laser with respect to the nanopost. A 10 nm lateral spatial displacement decreases the laser extinction ratio by one order of magnitude. For long acquisitions (autocorrelation function measurements), we periodically check the laser rejection and optimize it if necessary.

Finally, the RF signal is sent towards a monochromator which has a transmission window of 0.14 nm (50 GHz). This allows filtering out unwanted photoluminescence from other QDs (excited by the weak non-resonant laser) as well as the reflected non-resonant laser itself. The signal is then split with a 50/50 fibered beam splitter; the two exit paths are fed to superconducting nanowire single-photon detectors (SNSPDs, Single Quantum Eos). For the appropriate polarization (controlled with fibered paddle polarization controllers), the efficiency of these detectors at 930 nm exceeds 85%. They feature a dark count rate of about 50 Hz and a timing jitter lower than 20 ps (FWHM). Time tagging is provided by an acquisition card (Swabian instruments TimeTagger Ultra) that allows measuring count rates (linescan experiments) and coincidence counts (intensity autocorrelation measurements; total timing jitter of 35 ps (FWHM)).

## 1.2 Measurement procedure

For each laser power $P_{\mathrm{L}}$, we perform a linescan and an intensity autocorrelation measurement. A linescan contains 40 experimental points, for which the RF intensity is measured during 1 second. The total duration of one linescan is typically 1 minute. After the linescan, the laser is brought on resonance with the QD ($\omega_{\mathrm{L}} = \overline{\omega}_{eg}$) and the intensity autocorrelation is measured. Every 20 minutes, we perform a fast linescan to find the QD transition frequency $\overline{\omega}_{eg}$. This procedure allows for compensating for small fluctuations of $\omega_{eg}$. Finally, we optimize the laser rejection, the laser is brought on resonance with the QD ($\omega_{\mathrm{L}} = \overline{\omega}_{eg}$) and integration resumes for 20 min. The total duration of an intensity autocorrelation

measurement was 160 minutes per resonant power, for a total integration time of 65 hours.

# 2 Analytical model

This section presents the model used to jointly fit the linescan and intensity autocorrelation measurements. We first recall textbook results for an homogeneously-broadened two-level system that is quasi-resonantly driven by a laser. We next consider the separate impact of spectral diffusion and on/off blinking, assuming that these processes are slow compared to photon emission. We finally justify the expressions given in the main text. They are derived under the additional assumption that spectral diffusion and on/off blinking are statistically independent.

## 2.1 Homogeneously-broadened two-level system

We model the QD as a point-like two-level system (TLS) with a ground state $|g\rangle$ and an excited state $|e\rangle$. These two states are separated by an energy difference $\hbar\omega_{eg}$. The TLS is driven by a continuous wave laser, with an angular frequency $\omega_{\mathrm{L}} \approx \omega_{eg}$ and a negligible spectral linewidth. The TLS additionally experiences spontaneous emission and pure dephasing. The physical state of the TLS is represented by the density operator $\hat{\rho}$. In the rotating frame of light, and within the rotating wave approximation, the time evolution of $\hat{\rho}$ is governed by the master equation:

$$\frac{\mathrm{d}\hat{\rho}}{\mathrm{d}t} = -\frac{i}{\hbar}[\hat{H},\hat{\rho}] + \Gamma_1\big(\hat{\sigma}_-\hat{\rho}\hat{\sigma}_-^\dagger - \tfrac{1}{2}\{\hat{\sigma}_-^\dagger\hat{\sigma}_-,\hat{\rho}\}\big) + \frac{\Gamma^*}{2}\big(\hat{\sigma}_z\hat{\rho}\hat{\sigma}_z^\dagger - \tfrac{1}{2}\{\hat{\sigma}z^\dagger\hat{\sigma}_z,\hat{\rho}\}\big). \tag{1}$$

The first term describes the unitary dynamics associated with laser drive. $\hat{H}$ is the Hamiltonian of the driven TLS:

$$\frac{\hat{H}}{\hbar} = -\frac{1}{2}\delta\hat{\sigma}_z - \frac{1}{2}\Omega\hat{\sigma}_x. \tag{2}$$

Here, $\hat{\sigma}_z = |e\rangle\langle e| - |g\rangle\langle g|$ and $\hat{\sigma}_x = |g\rangle\langle e| + |e\rangle\langle g|$ are the Pauli operators; $\delta = \omega_{\mathrm{L}} - \omega_{eg}$ is the laser-emitter detuning; $\Omega$ (assumed to be a real number) is proportional to the amplitude of the driving electrical field. The second term in Eq. 1 describes the effect of spontaneous emission, which occurs at a rate $\Gamma_1$. The Lindblad operator is constructed with the jump operator $\hat{\sigma}_- = |g\rangle\langle e|$. The last term describes the effect of pure dephasing, with a rate $\Gamma^*$. The total dephasing rate $\Gamma_2$ features contributions from spontaneous emission and pure dephasing:

$$\Gamma_2 = \frac{\Gamma_1}{2} + \Gamma^*. \tag{3}$$

The population and coherence decay time are $T_1 = 1/\Gamma_1$ and $T_2 = 1/\Gamma_2$, respectively.

The state of the TLS is found by solving Eq. 1. An equivalent formulation is based on the components of the Bloch vector $(u, v, w)^\intercal = (2\mathrm{Re}(\rho_{eg}), 2\mathrm{Im}(\rho_{eg}), \rho_{gg} - \rho_{ee})^\intercal$. The associated optical Bloch equations read:

$$\begin{cases} \dot{u} = -\Gamma_2 u - \delta v \\ \dot{v} = \quad \delta u - \Gamma_2 v + \Omega w \\ \dot{w} = \qquad - \Omega v - \Gamma_1 w + \Gamma_1. \end{cases} \tag{4}$$

**Linescan.** In this experiment, one scans the laser angular frequency $\omega_{\mathrm{L}}$ across the TLS transition and measures the total scattered intensity $\langle I \rangle(\omega_{\mathrm{L}})$ (no spectral resolution on the detection). This intensity is proportional to the steady-state population of the excited state, $\rho_{ee,s}$. The latter is found by solving the optical Bloch equations in the steady-state, which yields:

$$\rho_{ee,s} = \frac{S}{2(1+S)} \times \frac{\Delta\omega_h^2}{4(\omega_{\mathrm{L}} - \omega_{eg})^2 + \Delta\omega_h^2}. \tag{5}$$

The first factor gives the population of the excited state for a resonant excitation ($\omega_{\mathrm{L}} = \omega_{eg}$). We introduced here the saturation parameter:

$$S = \frac{\Omega^2}{\Gamma_1 \Gamma_2}. \tag{6}$$

The second factor in Eq. 5 is a Lorentzian that describes the frequency dependence of $\rho_{ee,s}$. Its full width at half maximum (FWHM) is the homogeneous linewidth:

$$\Delta\omega_h = 2\Gamma_2\sqrt{1+S}. \tag{7}$$

**Intensity autocorrelation function.** Here, the angular frequency of the laser is fixed and one measures the second-order intensity correlation function $g^{(2)}(\tau)$ with a Hanbury-Brown and Twiss setup. Using Bayes theorem, $g^{(2)}(\tau)$ can be calculated as:

$$g^{(2)}(\tau) = \frac{\rho_{ee}(\tau)\big|_{\rho_{gg}(0)=1}}{\rho_{ee,s}}. \tag{8}$$

The numerator is obtained by solving the optical Bloch equations (Eq. 4) with the initial condition $\rho_{gg}(0) = 1$, or equivalently $(u, v, w)^\intercal(0) = (0, 0, 1)^\intercal$. These equations can be solved analytically (see *e.g.* Ref. S3; this reference uses a different convention for the definition of the Bloch vector and an opposite sign for the driving strength in the Hamiltonian).

## 2.2 Model for spectral diffusion

In this section, we consider a spectral diffusion process, which induces random changes of TLS frequency $\omega_{eg}$. We expand here on Refs. S4 and S5 to establish an analytical expression for the intensity autocorelation function that is valid for all delays.

**Model.** Specifically, we consider a Ornstein-Uhlenbeck process. The emitter frequency $\omega_{eg}$ undergoes a *continuous* diffusion process that is analogous to a random walk. This is a stationary, Markovian stochastic process. The probability distribution of $\omega_{eg}$ follows a Gaussian law:

$$\mathcal{G}(\omega_{eg}) = \frac{1}{\sqrt{2\pi}\Sigma} e^{-\frac{1}{2\Sigma^2}(\omega_{eg}-\overline{\omega}_{eg})^2}, \tag{9}$$

with $\overline{\omega}_{eg}$ the mean frequency and $\Sigma$ the standard deviation. The process is additionally characterized by the transition probability (Ref. S5, correction of a typo):

$$\mathcal{P}(\omega'_{eg}, t+\tau|\omega_{eg}, t) = \frac{1}{\sqrt{2\pi}\sigma(\tau)} \exp\left[-\frac{1}{2\sigma(\tau)^2}\left((\omega'_{eg}-\bar{\omega}_{eg}) - (\omega_{eg}-\bar{\omega}_{eg})e^{-\frac{|\tau|}{\tau_{\mathrm{SD}}}}\right)^2\right], \quad (10)$$

with

$$\sigma(\tau) = \Sigma\sqrt{1-e^{-\frac{2|\tau|}{\tau_{\mathrm{SD}}}}}. \quad (11)$$

For short delays ($|\tau| \ll \tau_{\mathrm{SD}}$), the TLS frequency does not have the time to change. As a consequence, the transition probability is equal to the Dirac delta-function $\delta(\omega'_{eg} - \omega_{eg})$. For long delays ($|\tau| \gg \tau_{\mathrm{SD}}$), the memory of the initial frequency is lost and the transition probability is equal to $\mathcal{G}(\omega'_{eg})$. The transition between these two regimes is controlled by the spectral diffusion time $\tau_{\mathrm{SD}}$. In all this work, we suppose that spectral diffusion is much slower than the dynamics of the TLS ($\tau_{\mathrm{SD}} \gg T_1, T_2$).

**Impact on linescans.** When spectral diffusion is much slower than the photon emission process, one can perform an adiabatic approximation. At a given time $t$, the population of the excited state is obtained by replacing $\omega_{eg}$ by $\omega_{eg}(t)$ in Eq. 5. For long integration times, assuming ergodicity, the collected intensity takes the form of a Voigt profile:

$$\langle\widetilde{I}\rangle(\omega_{\mathrm{L}}) \propto \int_{-\infty}^{+\infty} \mathrm{d}\omega_{eg}\mathcal{G}(\omega_{eg})\rho_{ee,s}(\omega_{eg}, \omega_{\mathrm{L}}). \quad (12)$$

The inhomogeneous broadening of the TLS lineshape is characterized by the inhomogeneous linewidth:

$$\Delta\omega_i = 2\sqrt{2\ln 2}\Sigma, \quad (13)$$

which corresponds to the FWHM of the probability density $\mathcal{G}(\omega_{eg})$.

**Impact on intensity autocorrelation.** In our intensity correlation measurements, the laser is resonant with the average transition frequency ($\omega_{\rm L} = \overline{\omega}_{eg}$). We treat in the following the general case for completeness. We note $\widetilde{g}^{(2)}(\tau)$ the intensity autocorrelation function in the presence of spectral diffusion. The condition $\tau_{\rm SD} \gg T_1, T_2$ allows us to distinguish two regimes.

- *Short delays* ($|\tau| \ll \tau_{\rm SD}$). Between the detection of a first photon at time $t$ and the detection of a second photon at $t+\tau$, $\omega_{eg}(t)$ is constant. One then obtains an 'instantaneous' coincidence rate:

$$\langle : I(t+\tau)I(t) : \rangle \propto \rho^2_{ee,s}(\omega_{eg}(t), \omega_{\rm L}) g^{(2)}(\omega_{eg}(t), \omega_{\rm L}, \tau). \tag{14}$$

A long measurement time yields the ensemble-averaged value:

$$\langle : \widetilde{I(t+\tau)I(t)} : \rangle \propto \int_{-\infty}^{+\infty} {\rm d}\omega_{eg} \mathcal{G}(\omega_{eg}) \rho^2_{ee,s}(\omega_{eg}, \omega_{\rm L}) g^{(2)}(\omega_{eg}, \omega_{\rm L}, \tau). \tag{15}$$

The steady-state average intensity is given by Eq. 12, which leads to:

$$\widetilde{g}^{(2)}(\tau) = \frac{\int {\rm d}\omega_{eg} \mathcal{G}(\omega_{eg}) \rho^2_{ee,s}(\omega_{eg}, \omega_{\rm L}) g^{(2)}(\omega_{eg}, \omega_{\rm L}, \tau)}{\left[ \int {\rm d}\omega_{eg} \mathcal{G}(\omega_{eg}) \rho_{ee,s}(\omega_{eg}, \omega_{\rm L}) \right]^2}. \tag{16}$$

In the main text, we used a more compact notation. The dependence on $\omega_{eg}$ and $\omega_{\rm L}$ is implicit. The ensemble averaging over the realizations of $\omega_{eg}$ using the probability distribution $\mathcal{G}(\omega_{eg})$ is noted $\langle ... \rangle$. Eq. 16 then reads:

$$\widetilde{g}^{(2)}(\tau) = \frac{\langle \rho^2_{ee,s} g^{(2)}(\tau) \rangle}{\langle \rho_{ee,s} \rangle^2} = \frac{\langle \rho^2_{ee,s} \rangle}{\langle \rho_{ee,s} \rangle^2} \times \frac{\langle \rho^2_{ee,s} g^{(2)}(\tau) \rangle}{\langle \rho^2_{ee,s} \rangle}. \tag{17}$$

In $g^{(2)}(\tau)$, the quantum features of the TLS (antibunching dip and Rabi oscillations for large driving powers) are visible for $|\tau|$ below a few $T_1, T_2$. In practice, $\widetilde{g}^{(2)}(\tau)$ features a similar short-delay behavior. This is due to the square dependence on the count rate, which favors

the situations in which the laser and the emitter are close to resonance. However, it is necessary to include spectral diffusion to obtain correct values for the parameters $T_2$ and $\Omega$ in the fit procedure. For $|\tau| \gg T_1, T_2$, one can ignore quantum correlations in the emission of the TLS ($g^{(2)}(\tau) = 1$). On then obtains $\widetilde{g}^{(2)}(\tau) = \frac{\langle \rho_{ee,s}^2 \rangle}{\langle \rho_{ee,s} \rangle^2} \geq 1$. This bunching behavior is due to fluctuations in the intensity of the TLS emission. The delay-dependence of the bunching peak is discussed in the next paragraph.

- *Long delays* ($|\tau| \gg T_1, T_2$). On this delay scale, we can ignore the quantum features associated with the emitter ($g^{(2)}(\tau) = 1$). However, when $|\tau| \sim \tau_{\mathrm{SD}}$, one should take into account the fluctuations of $\omega_{eg}$. Ensemble averaging then yields to the long-delay expression:

$$\widetilde{g}^{(2)}(\tau) = \frac{\iint \mathrm{d}\omega'_{eg} \mathrm{d}\omega_{eg} \mathcal{P}(\omega'_{eg}, t+\tau; \omega_{eg}, t) \rho_{ee,s}(\omega'_{eg}, \omega_{\mathrm{L}}) \rho_{ee,s}(\omega_{eg}, \omega_{\mathrm{L}})}{\left[ \int \mathrm{d}\omega_{eg} \mathcal{G}(\omega_{eg}) \rho_{ee,s}(\omega_{eg}, \omega_{\mathrm{L}}) \right]^2}. \tag{18}$$

The joint probability can be rewritten using Bayes' theorem:

$$\mathcal{P}(\omega'_{eg}, t+\tau; \omega_{eg}, t) = \mathcal{P}(\omega'_{eg}, t+\tau | \omega_{eg}, t) \mathcal{G}(\omega_{eg}). \tag{19}$$

Using the compact notation of the main text (implicit $\omega_{\mathrm{L}}$-dependence), Eq. 18 reads:

$$\begin{aligned} \widetilde{g}^{(2)}(\tau) &= \frac{1}{\langle \rho_{ee,s} \rangle^2} \iint \mathrm{d}\omega'_{eg} \mathrm{d}\omega_{eg} \mathcal{P}(\omega'_{eg}, t+\tau | \omega_{eg}, t) \mathcal{G}(\omega_{eg}) \rho_{ee,s}(\omega'_{eg}) \rho_{ee,s}(\omega_{eg}) \\ &= b_{\mathrm{SD}}(\tau). \end{aligned} \tag{20}$$

As pointed in Ref. S5, the apparent bunching time in $\widetilde{g}^{(2)}(\tau)$ depends on the ratio $\Delta\omega_h / \Delta\omega_i$ and is smaller than $\tau_{\mathrm{SD}}$.

- *A single expression for all delays.* The hierarchy $\tau_{\mathrm{SD}} \gg T_1, T_2$ makes it possible to capture the two previous cases in a single expression:

$$\widetilde{g}^{(2)}(\tau) = b_{\mathrm{SD}}(\tau) \times \frac{\langle \rho_{ee,s}^2 g^{(2)}(\tau) \rangle}{\langle \rho_{ee,s}^2 \rangle}. \tag{21}$$

## 2.3 Model for on/off blinking

In this section, we consider a TLS that features a bright ('on') state and a dark ('off') state. In the 'on' state the emitted average intensity is the one of the homogeneously-broadened TLS. In the 'off' state the intensity is zero. Random jumps between these two discrete states result in a blinking of the light emission.

**Model.** We suppose that the jumps between the 'on' and 'off' states occur at random times governed by a Poisson process. The mean lifetimes of the 'on' and 'off' states, $\tau_{\text{on}}$ and $\tau_{\text{off}}$, completely define the process. The steady-state probabilities of finding the system in the 'on' and 'off' states are:

$$\mathcal{P}(\text{on}) = \frac{\tau_{\text{on}}}{\tau_{\text{on}} + \tau_{\text{off}}} \qquad \text{and} \qquad \mathcal{P}(\text{off}) = \frac{\tau_{\text{off}}}{\tau_{\text{on}} + \tau_{\text{off}}}. \tag{22}$$

The transition probability from $i =$ 'on' or 'off' to $j =$ 'on' or 'off' is given by:

$$\mathcal{P}(j, t+\tau | i, t) = \mathcal{P}(j) + \big[\delta_{ji} - \mathcal{P}(j)\big] e^{-\frac{|\tau|}{\tau_{\text{on/off}}}}. \tag{23}$$

Here, $\delta_{ji}$ is the Kronecker symbol and $\tau_{\text{on/off}}$ is the blinking characteristic time:

$$\frac{1}{\tau_{\text{on/off}}} = \frac{1}{\tau_{\text{on}}} + \frac{1}{\tau_{\text{off}}}. \tag{24}$$

We now consider the impact of on/off blinking on linescans and on photon-photon correlations. Again, we assume that the on/off blinking dynamics is very slow compared to the TLS dynamics ($\tau_{\text{on/off}} \gg T_1, T_2$). The calculations follow the same logic as in the previous section, and this situation is discussed more often in the literature (see *e.g.* Ref. S6). Therefore, we will directly present the results.

**Linescan.** In the presence of on/off blinking, the average intensity is given by:

$$\langle \widetilde{I} \rangle(\omega_{\mathrm{L}}) \propto \mathcal{P}(\mathrm{on}) \rho_{ee,s}(\omega_{eg}, \omega_{\mathrm{L}}). \tag{25}$$

On/off blinking reduces the total intensity, but does not affect the spectral lineshape.

**Intensity autocorrelation.** Similarly than in the previous section, the short-delay ($|\tau| \ll \tau_{\mathrm{on/off}}$) and long-delay ($|\tau| \gg T_1, T_2$) limits are captured by a single formula:

$$\widetilde{g}^{(2)}(\tau) = b_{\mathrm{on/off}}(\tau) \times g^{(2)}(\tau), \tag{26}$$

with

$$b_{\mathrm{on/off}}(\tau) = 1 + \frac{\tau_{\mathrm{off}}}{\tau_{\mathrm{on}}} \exp\left( -\frac{|\tau|}{\tau_{\mathrm{on/off}}} \right). \tag{27}$$

## 2.4 Joint impact of spectral diffusion and on/off blinking

In this section, we consider the joint impact of spectral diffusion and on/off blinking. We use the same models as in sections 2.2 and 2.3. These processes are still slow compared to the TLS dynamics ($\tau_{\mathrm{SD}}, \tau_{\mathrm{on/off}} \gg T_1, T_2$). Furthermore, we assume statistical independence between spectral diffusion and on/off blinking. This allows factorizing all joint probabilities, which leads to the expressions given in the main text. They are recalled in the following for completeness.

**Linescan.** Up to a global scaling factor, the intensity collected during a linescan experiment is given by:

$$\langle \widetilde{I} \rangle(\omega_{\mathrm{L}}) \propto \mathcal{P}(\mathrm{on}) \int_{-\infty}^{+\infty} \mathrm{d}\omega_{eg} \mathcal{G}(\omega_{eg}) \rho_{ee,s}(\omega_{eg}, \omega_{\mathrm{L}}), \tag{28}$$

with $\mathcal{P}(\mathrm{on}) = \frac{\tau_{\mathrm{on}}}{\tau_{\mathrm{on}} + \tau_{\mathrm{off}}}$. On/off blinking decreases the collected intensity, but do not impact the spectral lineshape. Spectral diffusion induces a spectral broadening of the lineshape.

**Intensity autocorrelation.** We obtain a single expression that captures the joint impact of on/off blinking and spectral diffusion for all delays:

$$\widetilde{g}^{(2)}(\tau) = b_{\text{on/off}}(\tau) \times b_{\text{SD}}(\tau) \times \frac{\langle \rho_{ee,s}^2 g^{(2)}(\tau) \rangle}{\langle \rho_{ee,s}^2 \rangle}, \tag{29}$$

where $b_{\text{on/off}}(\tau)$ and $b_{\text{SD}}(\tau)$ are given by Eq. 27 and Eq. 20, respectively. This expression is discussed in the main text.

# 3 Fit process

In this section, we first discuss the fit of linescans and next present the complete fit process.

**Fit of linescans.** During a linescan, we measure the total intensity $I$ versus the frequency detuning between the laser and the QD. In this section, we present a quantitative comparison of the fit of linescans for a Gaussian, a Lorentzian, and a Voigt profile. In the first two cases, the fit parameters are free. In the last case, we employ the full model described in the main text, which also takes into account autocorrelation measurements (see next section for details). To ensure that the weight is evenly distributed between the central peak and the tails of the spectral line, we fit the logarithm (base 10) of the intensity. Figure S3 shows the fits for low-power ($P_{\text{L}} = 2.4\,\text{nW}$) and high-power ($P_{\text{L}} = 19\,\text{nW}$) data, which correspond to Fig. 2(a) in the main text. Both the Gaussian and Lorentzian functions fail at accurately describing the data (see the tails and the central peak, respectively), whereas the Voigt profile yields a much better result. The goodness of the fit can be quantified by the residual sum of squares: $\text{RSS} = \sum_k \left(\log_{10}(I_k^{\text{model}}) - \log_{10}(I_k^{\text{meas.}})\right)^2$. The values (see Fig. S3) confirm that Voigt profiles yield the best description.

**Complete fit process.** The fit parameters $T_2$ and $k = \Omega/\sqrt{P_{\text{L}}}$ are common to the complete data set (linescans and autocorrelation measurements for various laser powers). The

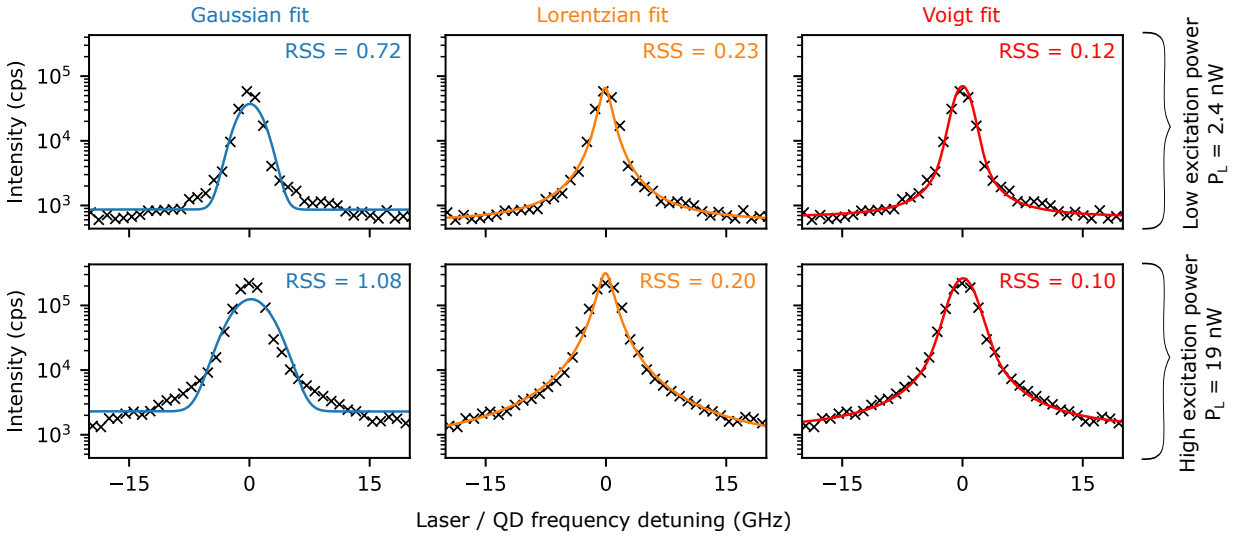


Figure S3: **Fit of experimental linescans to Gaussian, Lorentzian and Voigt profiles.** Crosses: raw experimental data for a low laser power ($P_{\mathrm{L}} = 2.4$ nW, top panels) and a high laser power ($P_{\mathrm{L}} = 19$ nW, bottom panels); the data are the one shown in the main text Fig. 2(a). Solid lines: fit to a Gaussian, Lorentzian and Voigt profiles (left, center and right column, respectively); RSS: residual sum of squares (see text for details).

parameters of spectral diffusion ($\Sigma$ and $\tau_{\mathrm{SD}}$) and on/off blinking ($\tau_{\mathrm{on}}$ and $\tau_{\mathrm{off}}$) are adjusted for each laser power. We fit the data using a fitting "loop", which allows converging to the values of $k$ and $T_2$ after a few iterations.

We start the first "loop" by fitting the linescans with an unrestricted Voigt function, allowing us to extract starting values for the emission maximal intensity, the homogeneous linewidth $\Delta\omega_h$, and the inhomogeneous linewidth $\Delta\omega_i$. We extract from $\Delta\omega_h = 2T_2^{-1}\sqrt{1+\Omega^2 T_1 T_2}$ starting values for the coherence time $T_2$ and for $k = \Omega/\sqrt{P_{\mathrm{L}}}$.

Secondly, we consider the "long delay" autocorrelation function. Knowing $T_2$ and $\Delta\omega_i$, we can calculate the bunching amplitude induced by the spectral diffusion for all laser powers: $b_{\mathrm{SD}}(0) = \frac{\langle\rho_{ee,s}^2\rangle}{\langle\rho_{ee,s}\rangle^2}$. We then fit the long delay autocorrelation function and find the characteristic time of the spectral diffusion process $\tau_{\mathrm{SD}}$, as well as the on/off blinking bunching amplitude $b_{\mathrm{on/off}}(0) = \frac{\tau_{\mathrm{on}}+\tau_{\mathrm{off}}}{\tau_{\mathrm{on}}}$ and characteristic time $\tau_{\mathrm{on/off}} = \left(\tau_{\mathrm{on}}^{-1} + \tau_{\mathrm{off}}^{-1}\right)^{-1}$, for all laser powers.

Thirdly, we consider the "short delay" autocorrelation function. We fit the data, by

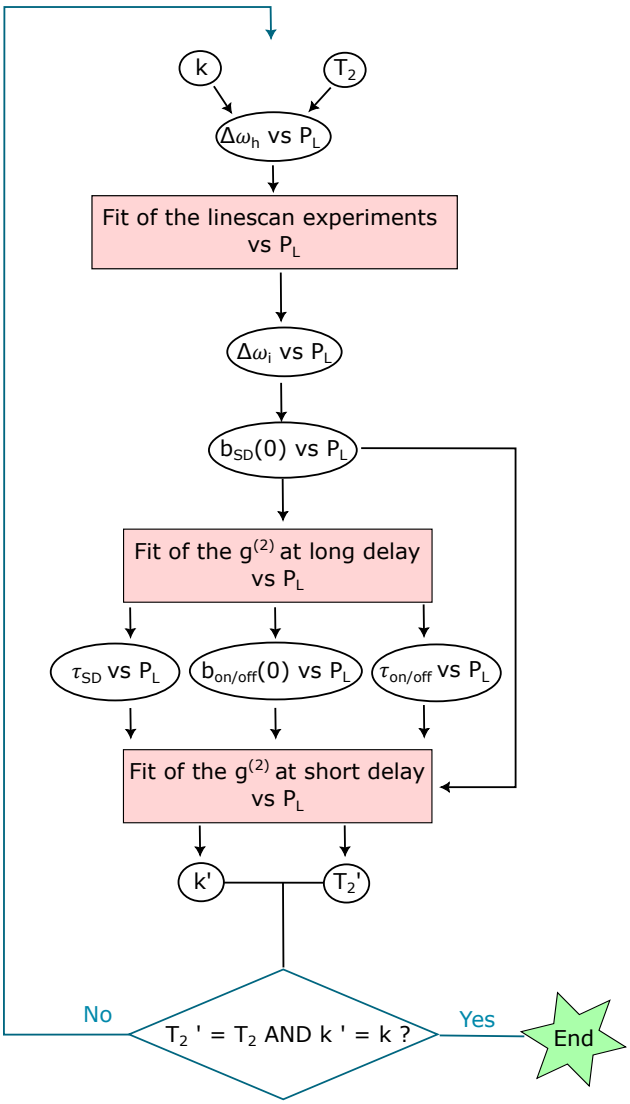


Figure S4: **Data refinement loop process.** The rectangles show which data is fitted, and the circles which parameters are extracted from the fit.

imposing $k$ and $T_2$ as shared parameters for all datasets. Furthermore, we fix $\Delta\omega_i$, $b_{\mathrm{SD}}(0)$, $b_{\mathrm{on/off}}(0)$, $\tau_{\mathrm{SD}}$ and $\tau_{\mathrm{on/off}}$ to the value found during the first and second fitting steps described above. We note that the short delay autocorrelation function is very sensitive on the Rabi frequency at high excitation powers, which allows a fast convergence of the estimation of $k$.

Finally, we compare the refined values of $T_2$ and $k$ with the ones given by the fit of the linescans. If the values are different (with a $\sim 1\%$ tolerance), we inject the newly found values of $T_2$ and $k$ at the beginning of the process, calculate the value of $\Delta\omega_h$ for all values of $P_{\mathrm{L}}$ and perform the refinements again. Figure S4 summarizes the "loop" fitting process.

At the end of the process, we find a set of parameters that describe all the data using our analytical model. We find a coherence time $T_2 = 490\,\mathrm{ps} = 0.7 \times 2T_1$ and a factor $k = 2\pi \times 122\,\frac{\mathrm{MHz}}{\sqrt{\mathrm{nW}}}$.

# 4 Effect of the non-resonant auxiliary excitation

In this section, we discuss the impact of non-resonant excitation on the QD resonance fluorescence. Throughout the section, the resonant excitation power is set to $P_{\mathrm{L}} = 9\,\mathrm{nW}$. These preliminary measurements were performed without the monochromator. Therefore, the photoluminescence from all the QDs in the nanopost — excited by the non-resonant laser — contributes to a constant background signal. The background level in the presence of the monochromator will be discussed in section 5.

Figure S5(a) shows a series of linescans for increasing values of the non-resonant power $P_{\mathrm{nr}}$. For $P_{\mathrm{nr}} = 0$, we cannot observe any resonance fluorescence from the QD. Increasing $P_{\mathrm{nr}}$ leads to a dramatic increase in the RF counts, already visible for $P_{\mathrm{nr}} = 14\,\mathrm{nW}$. The weak non-resonant laser acts as a "switch" for the resonance fluorescence signal. This "gate" effect is well described in the literature (see for instance references S7 and S8). The non-resonant laser stabilizes the charge state of the QD, enabling the resonant excitation of the transition. To gain quantitative insights, we fit the data with a Voigt function plus a flat background.

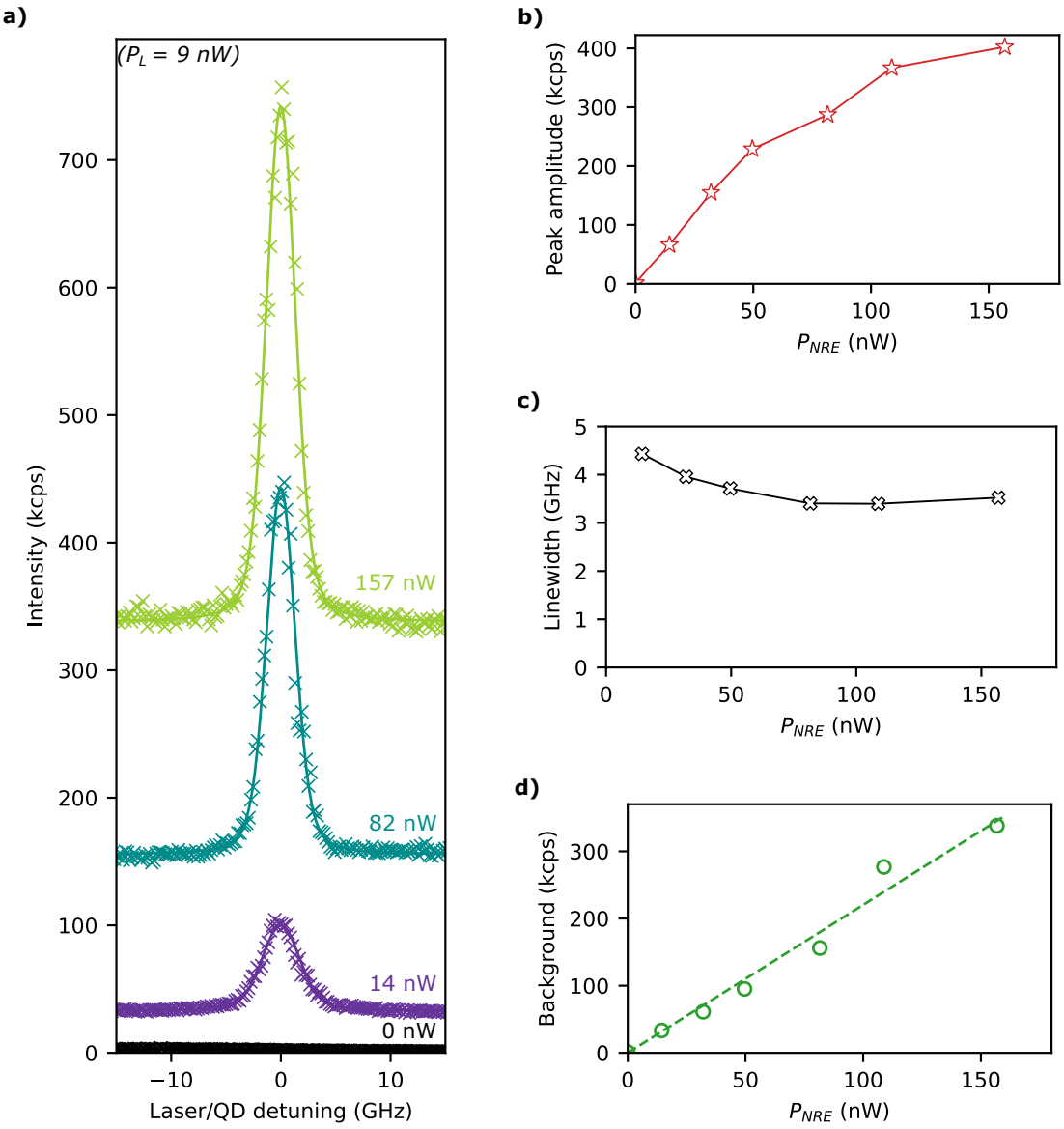


Figure S5: **Impact of non-resonant excitation.** (a) Intensity as a function of the laser-QD detuning (linescans) for various non-resonant excitation powers ($P_{\mathrm{nr}}$). Crosses: raw experimental data, solid line: fit to a Voigt profile plus a constant background. The fit yields the amplitude of the RF peak, the total linewidth (FWHM) and the background level. These quantities are plotted against $P_{\mathrm{nr}}$ in panels (b), (c) and (d), respectively. The *resonant* laser power is set to $P_{\mathrm{L}} = 9$ nW; no monochromator for these measurements.

This analysis yields the RF signal at resonance (panel (b)), the total linewidth (FWHM, panel (c)) and the background level (panel (d)).

Figure S5(b) shows that the RF signal increases to $400 \times 10^3$ counts per second for $P_{\mathrm{nr}} = 157$ nW. The curve also displays a saturation. In Fig. S5(c), we observe that the

non-resonant illumination also reduces the total linewidth by about 25%. This reduction saturates for $P_{\mathrm{nr}} \geq 80\,\mathrm{nW}$ (before saturation of the RF intensity). We believe that the free carriers created by the non-resonant illumination also stabilize the charge environment of the QD, thus reducing spectral diffusion. Figure S5(d) shows that the background level strongly increases with $P_{\mathrm{nr}}$. This is expected: the non-resonant laser excites the photoluminescence of all the QDs embedded in the nanopost cavity.

In the main text, we set the non-resonant power to $P_{\mathrm{nr}} = 160\,\mathrm{nW}$. Increasing further $P_{\mathrm{nr}}$ leads to a marginal gain in RF intensity, while significantly increasing the background level. The background level in the presence of the monochromator is discussed in the next section.

# 5 Background level

In this section, we discuss the background level, in the presence of a monochromator (configuration used for the experiments presented in the main text). Here, the power of the non-resonant laser is set to $P_{\mathrm{nr}} = 160\,\mathrm{nW}$. The monochromator suppresses the background photoluminescence of all QDs, but the trion line under investigation (spectral width of the transmission window: 0.14 nm). In these conditions, the background counts feature two contributions: i) the photoluminescence of the transition of interest, excited by the weak, *non-resonant* laser and ii) residual stray light associated with the *resonant* laser, due to imperfect polarization rejection. These two contributions are apparent in Fig. S6, which shows the background level as a function of the power $P_{\mathrm{L}}$ of the resonant laser. The zero-power limit yields the contribution of the photoluminescence induced by the non-resonant laser (700 cps). Compared to the unfiltered case (see Fig. S5(d)), the photoluminescence background level is decreased by a factor of 400. The contribution due to imperfect polarization filtering increases linearly with $P_{\mathrm{L}}$ (slope: 60 cps/nW).

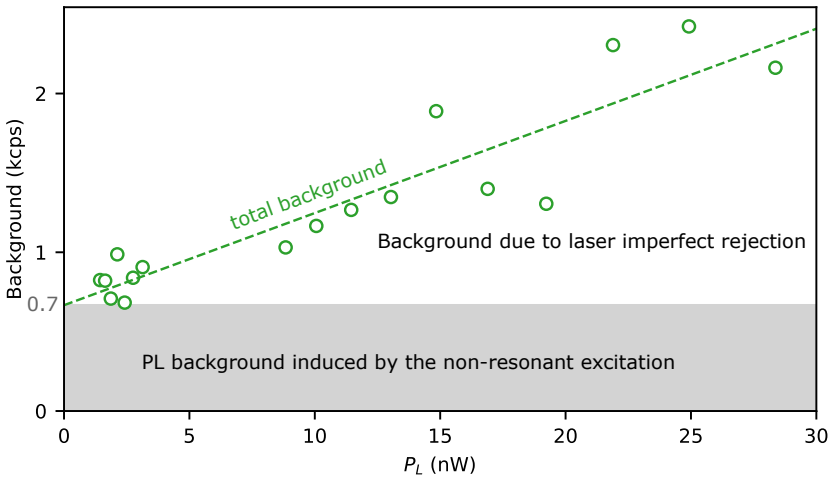


Figure S6: **Background counts versus the power of the resonant laser**. The non-resonant power is set to $P_{\mathrm{nr}} = 160\,\mathrm{nW}$.

# 6 Measurement of the lifetime $T_1$

The lifetime of the excited state was measured using a pulsed, non-resonant laser (wetting layer excitation). We used a small power (10% of the saturation power) in order to minimize the population of higher-energy excitonic complexes. The QD luminescence was directed towards a fast avalanche photodiode (Id Quantique 100-50). The instrumental response function (IRF) is shown in Fig. S7. It features a timing jitter of $180 \pm 15\,\mathrm{ps}$ (FWHM), which is here dominated by the contribution of the acquisition card. The experimental data, shown in Fig. S7, are fitted to the convolution of a single exponential decay with the IRF. This procedure yields a lifetime $T_1 = 350 \pm 25\,\mathrm{ps}$.

Due to the broadband operation of the nanopost, we cannot quantify the Purcell acceleration by tuning the investigated QD on- and off-resonance. Instead, we compare the radiative lifetime of this QD with the one of an ensemble of similar QDs embedded in bulk GaAs. As described in Ref. S9, we measured the lifetime of an ensemble of QDs embedded in large squares ($20\,\mu\mathrm{m} \times 20\,\mu\mathrm{m}$) that are patterned on the same chip as nanoposts. Next, we correct for the small acceleration of spontaneous emission provided by the planar structure (calculated acceleration : $\times 1.32$). This yields a reference lifetime of 1.66 ns for InAs QDs

in bulk GaAs. The QD investigated in this work thus features a Purcell acceleration by a factor of 4.8, close to the maximum value (calculated $F_P = 6.3$ for this structure[S9]).

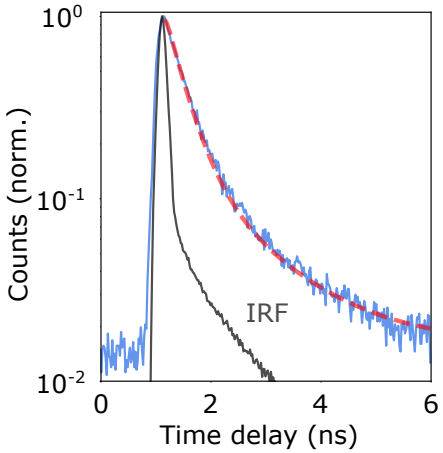


Figure S7: **Lifetime measurement.** The measurement points (blue solid line) are fitted to a single exponential decay convoluted with the instrumental response function (IRF, solid black line). The fit (red dashed line) yields a lifetime $T_1 = 350 \pm 25$ ps.

# References


(S1) Kuhlmann, A. V.; Houel, J.; Brunner, D.; Ludwig, A.; Reuter, D.; Wieck, A. D.; Warburton, R. J. A dark-field microscope for background-free detection of resonance fluorescence from single semiconductor quantum dots operating in a set-and-forget mode. Rev. Sci. Instrum. **2013**, 84, 073905.

(S2) Mansuripur, M. Effects of high-numerical-aperture focusing on the state of polarization in optical and magneto-optic data storage systems. Applied Optics **1991**, 30, 3154.

(S3) Noh, H.-R.; Jhe, W. Analytic solutions of the optical Bloch equations. Optics Communications **2010**, 283, 2353–2355.

(S4) Fournier, C.; Watanabe, K.; Taniguchi, T.; Barjon, J.; Buil, S.; Hermier, J.-P.; Delteil, A. Investigating the fast spectral diffusion of a quantum emitter in hBN using resonant excitation and photon correlations. Phys. Rev. B **2023**, 107, 195304.

(S5) Delteil, A.; Buil, S.; Hermier, J.-P. Photon statistics of resonantly driven spectrally diffusive quantum emitters. Phys. Rev. B **2024**, 109, 155308.

(S6) Jahn, J.-P.; Munsch, M.; Béguin, L.; Kuhlmann, A. V.; Renggli, M.; Huo, Y.; Ding, F.; Trotta, R.; Reindl, M.; Schmidt, O. G.; Rastelli, A.; Treutlein, P.; Warburton, R. J. An artificial Rb atom in a semiconductor with lifetime-limited linewidth. Phys. Rev. B **2015**, 92, 245439.

(S7) Nguyen, H. S.; Sallen, G.; Voisin, C.; Roussignol, P.; Diederichs, C.; Cassabois, G. Optically Gated Resonant Emission of Single Quantum Dots. Phys. Rev. Lett. **2012**, 108, 057401.

(S8) Nguyen, H. S.; Sallen, G.; Abbarchi, M.; Ferreira, R.; Voisin, C.; Roussignol, P.; Cassabois, G.; Diederichs, C. Photoneutralization and slow capture of carriers in quantum dots probed by resonant excitation spectroscopy. Phys. Rev. B **2013**, 87, 115305.

(S9) Kotal, S.; Artioli, A.; Wang, Y.; Osterkryger, A. D.; Finazzer, M.; Fons, R.; Genuist, Y.; Bleuse, J.; Gérard, J.-M.; Gregersen, N.; Claudon, J. A nanowire optical nanocavity for broadband enhancement of spontaneous emission. Appl. Phys. Lett. **2021**, 118, 194002.